

1 **Dynamic PRC1-CBX8 stabilizes a porous structure of chromatin condensates**

2 Michael Uckelmann¹, Vita Levina¹, Cyntia Taveneau^{1,2}, Xiao Han Ng¹, Varun Pandey³,
3 Jasmine Martinez⁴, Shweta Mendiratta⁴, Justin Houx⁵, Marion Boudes¹, Hari Venugopal⁶,
4 Sylvain Trépout⁶, Qi Zhang¹, Sarena Flanigan¹, Minrui Li^{1,7}, Emma Sierecki⁵, Yann Gambin⁵,
5 Partha Pratim Das³, Oliver Bell⁴, Alex de Marco^{1,2,8}, Chen Davidovich^{1,9*}

6 ¹ Department of Biochemistry and Molecular Biology, Biomedicine Discovery Institute,
7 Faculty of Medicine, Nursing and Health Sciences, Monash University; Clayton, Victoria,
8 3800, Australia.

9 ² ARC Centre of Excellence in Advanced Molecular Imaging, Monash University; Clayton,
10 Victoria, 3800, Australia.

11 ³ Department of Anatomy and Developmental Biology, Development and Stem Cells
12 Program, Monash Biomedicine Discovery Institute, Monash University; Clayton, Victoria,
13 3800, Australia.

14 ⁴ Departments of Biochemistry and Molecular Medicine, and Stem Cell and Regenerative
15 Medicine, Norris Comprehensive Cancer Center, Keck School of Medicine, University of
16 Southern California, Los Angeles, CA 90033, USA.

17 ⁵ EMBL Australia Node for Single Molecule Science and School of Biomedical Sciences,
18 Faculty of Medicine, The University of New South Wales, Sydney, NSW, 2052 Australia.

19 ⁶ Ramaciotti Centre for Cryo-Electron Microscopy, Monash University, Monash, Victoria,
20 Australia.

21 ⁷ Faculty of Information Technology, Monash University; Clayton, Victoria, 3800, Australia.

22 ⁸ Simons Electron Microscopy Center, New York Structural Biology Center, New York 10027
23 NY, United States of America

24 ⁹ EMBL-Australia; Clayton, Victoria, 3800, Australia.

25 * Correspondence: Chen.Davidovich@monash.edu

26 **Abstract**

27 The compaction of chromatin is a prevalent paradigm in gene repression. Chromatin
28 compaction is commonly thought to repress transcription by restricting chromatin
29 accessibility. However, the spatial organisation and dynamics of chromatin compacted by
30 gene-repressing factors are unknown. Using cryo-electron tomography, we solved the three-
31 dimensional structure of chromatin condensed by the Polycomb Repressive Complex 1
32 (PRC1) in a complex with CBX8. PRC1-condensed chromatin is porous and stabilised through
33 multivalent dynamic interactions of PRC1 with chromatin. Mechanistically, positively
34 charged residues on the internally disordered regions (IDRs) of CBX8 mask negative charges

35 on the DNA to stabilize the condensed state of chromatin. Within condensates, PRC1
36 remains dynamic while maintaining a static chromatin structure. In differentiated mouse
37 embryonic stem cells, CBX8-bound chromatin remains accessible. These findings challenge
38 the idea of rigidly compacted polycomb domains and instead provides a mechanistic
39 framework for dynamic and accessible PRC1-chromatin condensates.

40 **Main**

41 Chromatin structure is intricately linked to transcriptional activity¹. Compacted or “closed”
42 chromatin is generally associated with inhibition of transcription while “open”, more
43 accessible chromatin is more prone to being transcribed¹. Polycomb Repressive Complex 1
44 (PRC1) is a repressive chromatin modifier critical for organismal development^{2,3}. PRC1 has
45 been proposed to inhibit gene expression by tightly compacting chromatin in a process that
46 often is considered to restrict chromatin accessibility²⁻¹¹. However, direct evidence for
47 PRC1-compacted chromatin being inaccessible is sparse and mechanistic explanations
48 remain unsatisfactory (reviewed in¹¹). Furthermore, recent studies show that changes in
49 chromatin accessibility are more gradual than the simple binary classification into “open”
50 and “closed” chromatin suggests¹²⁻¹⁵. A challenge in consolidating these seemingly
51 contradictory findings is limited information into how PRC1 influences the three dimensional
52 structure of chromatin.

53 PRC1 complexes can include one of five different chromobox proteins (CBX), all homologous
54 to the fly Polycomb (Pc)¹⁶. The CBX protein CBX2 forms condensates through liquid-liquid
55 phase separation, providing a potential mechanism for the compartmentalization of
56 facultative heterochromatin^{9,10}. Phase separation is emerging as a mechanism for chromatin
57 organisation through the association of self-similar domains¹⁷. Chromatin can form
58 condensates in the presence of divalent cations and histone tails¹⁷⁻²⁰. Within these
59 condensates, chromatin has variably been described as liquid-like, formed through liquid-
60 liquid phase separation^{17,19}, or as solid²⁰. A recent structure of liquid-liquid phase-separated
61 chromatin, condensed by magnesium cations without protein binding partners, revealed
62 that nucleosomes organise into irregular assemblies¹⁹. The lack of apparent periodicity in
63 chromatin geometry has also been noted in computational simulations and in first attempts
64 to image chromatin in cells by cryo-electron tomography (cryo-ET)^{21,22}. However, the
65 structural arrangement of chromatin condensed by a repressive factor remained unknown.

66 Herein we describe the three dimensional cryo-ET structure of chromatin condensed by a
67 polycomb-repressive complex. We focus on a PRC1 complex that includes CBX8 (PRC1^{C8}), a
68 chromobox protein that is upregulated during cell differentiation²³ and has oncogenic
69 potential^{24,25}. We show that dynamic interactions between PRC1^{C8} and chromatin promote
70 condensates through phase separation. Mechanistically, positive charges on the internally
71 disordered regions (IDRs) of CBX8 are required for DNA binding and chromatin
72 condensation. Contrary to expectations, PRC1-condensed chromatin is not tightly

73 compacted but stabilises a porous chromatin structure that allows largely unhindered
74 diffusion of PRC1^{C8}.

75 **Results**

76 **PRC1-chromatin condensates are porous and accessible**

77 To determine the structure of polycomb-compacted chromatin and the mechanisms of
78 polycomb-driven chromatin compaction, we reconstituted the system *in vitro*. The
79 reconstitution included a chromatinized polycomb target gene (3,631 bp DNA) with a
80 sequence from the human ATOH1 locus, which can harbour roughly up to 20 nucleosomes,
81 assuming 150-200 bp per nucleosome. This construct is referred to as chromatin hereafter.
82 We used a native DNA sequence for chromatin reconstitution, as regular spacing using
83 artificial nucleosome stabilising sequences were previously reported to drive the liquid-
84 liquid phase separation of chromatin¹⁷. The nucleosomes on the chromatin that we
85 reconstituted are not evenly phased (Extended Data Fig. 1a). The purified recombinant PRC1
86 complex is composed of RING1B, BMI1 and CBX8 (PRC1^{C8}) (Fig. 1a). The PRC1^{C8} complex is
87 pure (Fig. 1b), monodispersed (Fig. 1c) and retains H2A ubiquitylation activity comparable to
88 the RING1b-BMI1 heterodimer (Fig. 1d). This also applies to all other protein complexes
89 used in this study (Extended Data Fig. 2 and 1b,c).

90 When combined, chromatin and PRC1^{C8} were sufficient to form spherical phase-separated
91 condensates, apparent in differential interference contrast (DIC) and fluorescence imaging
92 (Fig. 1e). Using two different fluorescence labels, we confirmed the presence of both
93 chromatin and PRC1^{C8} within the same condensates (Fig. 1e). Importantly, both PRC1^{C8} and
94 chromatin are necessary for chromatin condensation, while the individual components do
95 not phase-separate (Fig. 1e). PRC1^{C8}-chromatin condensates are preserved on an EM grid
96 after vitrification (Fig. 1f). To study these structures by cryo-electron tomography, we
97 reduced the salt concentration and increased chromatin concentration (see Methods
98 section). This was done to decrease condensate size and abundance, which was necessary
99 for high-quality data collection (Fig. 1g). We used a PRC1 complex with MBP-tagged CBX8
100 for cryo-tomography. The MBP tag does not affect condensation, as condensates still form
101 after tag cleavage (Extended Data Fig. 1d). We collected tomograms near the borders of a
102 condensates, to observe the boundary conditions (Extended Data Fig. 3a for an example of a
103 condensate on the grid). Subtomogram averaging allowed us to identify the orientation and
104 position of individual nucleosomes in the tomographic volume (Extended Data Fig. 3b-d).
105 The reconstruction reveals a dense network of hundreds of nucleosomes with a distinct
106 condensate boundary (Fig. 1g and Movie S1). We could not unambiguously assign density to
107 PRC1^{C8}, possibly because it adapts various conformations while simultaneously using
108 multiple surfaces to interact with chromatin (more below). The final structure reflects the
109 arrangement of nucleosomes in PRC1^{C8}-chromatin condensate (Fig. 1g, second panel).
110 Unexpectedly, the structure shows that PRC1^{C8} does not compact nucleosomes into an

111 impassable barrier. Instead, PRC1^{C8} rather stabilises chromatin in a porous mesh-like
112 structure (Fig. 1g). Analysing the orientation of individual nucleosomes towards their
113 neighbouring nucleosomes shows no obvious orientation bias (Extended Data Fig. 3c,d). We
114 conclude that PRC1^{C8} does not induce a substantial inter-nucleosome orientation bias, but
115 rather supports forming a porous chromatin structure.

116 We next wished to determine the size of macromolecules that could diffuse into PRC1-
117 chromatin condensates. We used the condensate structure to calculate solvent-excluded
118 volumes²⁶ with variable probe radii ranging from 0.2 nm to 20 nm (Fig. 1h,i). Interestingly,
119 the analysis shows that the condensate is accessible for macromolecules of a considerable
120 size of up to 8 nm in radius (equivalent to approximately 600 kDa). Small macromolecules
121 (<10 kDa), with radii below 2 nm, would have enough room to access every single
122 nucleosome. Conversely, access is increasingly restricted for molecules with a radius above
123 8 nm (approximately 600 kDa). This suggests that PRC1-chromatin condensates are
124 surprisingly accessible and that PRC1^{C8} itself would be able to move within these
125 condensates largely unhindered.

126 To compare the structure of PRC1^{C8}-chromatin condensates to PRC1^{C8}-free chromatin, we
127 generated cryo-tomograms of chromatin without PRC1^{C8} (Fig. 1j, movie S2). Low
128 magnification cryo-EM images show that condensation happens only in the presence of
129 PRC1^{C8} (Extended Data Fig. 4a,b) and condensates are preserved on the EM grid. The
130 structure of chromatin in the absence of PRC1^{C8} is less dense than in the presence of PRC1^{C8},
131 with distances between neighbouring nucleosomes that are on average significantly longer
132 (Fig. 1j,k). These results confirm that PRC1^{C8} facilitates large-scale chromatin restructuring.

133 We observe some sporadic areas of high nucleosome density, even without PRC1 (Extended
134 Data Fig. 4c,d). The median distance to the next neighbouring nucleosomes in these
135 sporadic dense PRC1^{C8}-free condensates are very similar to distances measured in the
136 PRC1^{C8}-chromatin condensates (9.8 nm and 10.9 nm, respectively, Extended Data Fig. 4d).
137 This matches closely to distances reported for chromatin condensed by MgCl₂, where the
138 radial distribution function of nucleosomes peaked at 10.6 nm¹⁹. At the nuclear periphery in
139 cells, the median distance between neighbouring nucleosomes is about 12 nm, which is
140 again remarkably similar²⁷. Overall, this raises the possibility that PRC1 thermodynamically
141 stabilises a naturally-occurring condensed chromatin state, rather than actively compacts
142 chromatin. By doing so, PRC1 may cause multiple compacted arrays to cluster together
143 more often.

144 **PRC1^{C8} is mobile and chromatin is static within PRC1-chromatin condensates**

145 To gain further insights into PRC1^{C8}-chromatin condensation, we tested the dependency of
146 condensation on the concentration of PRC1 and chromatin. Condensates form under close
147 to physiological monovalent salt concentrations of 122.5 mM (90 mM KCl and 32.5 mM

148 NaCl), at PRC1^{C8} concentrations as low as 250 nM and are dependent on PRC1^{C8} (Fig. 2a). At
149 a high concentration of PRC1^{C8} (2,000 nM), most efficient condensation occurs at high
150 chromatin concentration (850 nM nucleosome concentration). Yet, at lower concentration
151 of PRC1^{C8} (250 nM), ideal condensation appears at lower chromatin concentration and the
152 condensation efficiency is then reduced when the chromatin concentration increases (Fig
153 2a). This is possibly because at high chromatin concentration the large amount of potential
154 binding sites for PRC1^{C8} reduces the average per-site-occupancy of PRC1^{C8}. This may lead to
155 less efficient phase separation. A similar observation was recently made for a PRC1 complex
156 with CBX2 and PHC2²⁸. Altering the salt concentrations confirms that PRC1^{C8}-chromatin
157 condensates most readily form close to physiological salt concentration (Extended Data Fig.
158 5). We conclude that PRC1^{C8} is sufficient to drive the formation of the chromatin
159 condensates under physiologically relevant conditions. Furthermore, the efficiency of phase
160 separation depends on the ratio of PRC1 to chromatin. We next asked if chromatin and
161 PRC1 show different dynamics within the condensates.

162 Fluorescence recovery after photobleaching (FRAP) of PRC1^{C8}-chromatin condensates shows
163 fast recovery kinetics for GFP-labelled PRC1 (Fig. 2b, in green; $T_{1/2} = 71 \pm 8$ s). Conversely, we
164 observed a very slow recovery for Cy5-labelled chromatin (Fig. 2b, in red). The GFP signal
165 does not recover up to 100 % but rather plateaus at $72 \pm 2\%$. This is possibly because a
166 substantial percentage of the condensate has been bleached, while redistribution of GFP-
167 labelled PRC1^{C8} within the same condensate likely drives fluorescence recovery during the
168 monitored timescale. However, we cannot exclude the possibility that incomplete recovery
169 is due to an immobile fraction of CBX8. To exclude the possibility that a large protein tag on
170 CBX8 prevents it from remaining static on chromatin we used a synthetic fluorescence dye
171 to sparsely label random lysine residues of PRC1^{C8}. We then compared FRAP recovery for
172 two different PRC1 complexes: one complex included CBX8 with an N-terminal MBP tag and
173 the other included an untagged CBX8 (Extended Data Fig. 6a,b). The PRC1^{C8} with untagged
174 CBX8 is still dynamic (Extended Data Fig. 6a, $T_{1/2} = \sim 1300$ s), albeit recovery is slower when
175 compared to MBP-tagged PRC1^{C8} (Extended Data Fig. 6b, $T_{1/2} = 362 \pm 29$ s) and the GFP-
176 tagged protein (Fig. 2b; $T_{1/2} = 71 \pm 8$ s). Chromatin remains static in all samples. These
177 results indicate that although the tagging and labelling strategies affect the dynamics of the
178 system quantitatively, its overall behaviour remains qualitatively the same: within
179 condensates, PRC1 is mobile while chromatin itself is static (Fig. 2c and Extended Data Fig.
180 6). This confirms that PRC1^{C8} can diffuse within PRC1^{C8}-chromatin condensates, in line with
181 our structural analysis (Fig. 1h,i). Recent publications have been at odds as to the solid or
182 liquid state of chromatin^{17,20}. Our data suggests that chromatin behaves as a solid-like
183 material when condensed by PRC1^{C8}.

184 We next wished to gain insights into PRC1^{C8} -chromatin condensate formations at low
185 protein concentrations that better resemble physiological concentrations. To this end, we
186 employed a single-molecule confocal microscope that allows tracking of individual
187 condensates through a confocal volume²⁹ (Extended Data Fig. 7a,b). We used GFP-labelled

188 PRC1^{C8}, where GFP peaks indicate the formation of bright protein assemblies. Importantly,
189 this system allows the detection of protein assemblies smaller than what can be identified
190 by standard fluorescence microscopes³⁰. In the presence of chromatin, assemblies are
191 observed at PRC1^{C8} concentrations as low as 62.5 nM (Extended data Fig. 7c). This indicates
192 that condensates can form at physiologically relevant PRC1 concentrations, previously
193 estimated as 130 nM in polycomb bodies in cells³¹. In the absence of chromatin, GFP peaks
194 are only detected sporadically, even at the highest PRC1^{C8} concentration (Extended Data Fig.
195 7 b,c). Overall, this data indicates that PRC1^{C8}-chromatin condensates form under
196 physiologically relevant PRC1^{C8} concentration, but do not form without chromatin.

197 **Multivalent interactions between PRC1^{C8} and chromatin induce phase separation**

198 A scaffold-client based phase separation model has recently been proposed for PRC1-CBX2
199 complexes^{28,35}, where CBX2³⁵ or chromatin²⁸ act as a scaffold that induces phase separation
200 of PRC1 proteins. Since PRC1^{C8} is insufficient to phase-separate without chromatin (Fig 1e),
201 we wished to test if chromatin might act as a scaffold that concentrates PRC1^{C8} and induces
202 phase separation. To test this model, we probed the different interaction sites between
203 PRC1 and chromatin. The whole PRC1^{C8} complex (RING1b, BMI1 and CBX8) is necessary and
204 sufficient to condense chromatin, while the PRC1 core or CBX8 alone do not condense
205 chromatin (Fig. 3a). This suggests multivalent interactions between the PRC1^{C8} complex and
206 chromatin, involving different chromatin interacting surfaces in both PRC1 and CBX8. To
207 identify the different interaction sites, we first used crosslinking mass spectrometry (XL-MS)
208 to probe for protein-protein interactions within PRC1^{C8}-chromatin condensates (Fig. 3b and
209 Supplementary Data 4; PRC1 with an MBP-tagged CBX8 was used). As expected, we
210 identified extensive crosslinks between the RING domains of RING1B and BMI1. RING1B and
211 BMI1 did not crosslink to histones. This is likely because these proteins bind to the acidic
212 patch of the nucleosome³⁶, which is unlikely to be crosslinked by the BS3 crosslinker that
213 reacts preferentially with lysine residues. The results show multiple crosslinks from the CBX8
214 chromodomain to the H3 histone tail (Fig. 3b), indicative of binding. Interactions between
215 CBX-proteins and H3K27me3-modified H3-histone tails have been proposed to recruit PRC1
216 to chromatin modified by PRC2^{2,3}. However, CBX8 did crosslink to unmethylated H3 tails
217 (Fig. 3b) and a trimethyl-lysine analogue (MLA) at H3K27 did not improve the chromatin-
218 condensation activity of PRC1^{C8} (Fig. 3d). We conclude that H3K27me3 is not necessary for
219 the chromatin condensation activity of PRC1^{C8} and that the H3 histone tail, even if
220 unmodified, provides an interaction site for PRC1 on chromatin.

221 We also observe extensive self-crosslinks in the IDRs of CBX8 (Fig. 3b). This may indicate
222 inter- or intramolecular interaction within this flexible lysine-rich region. However, these
223 self-crosslinks within the IDRs appear even in the absence of chromatin, suggesting that
224 they are not related to condensation (Extended Data Fig. 8 and Supplementary Data 3).

225 DNA has previously been shown to bind CBX8³⁷ and could provide another interaction site
226 for PRC1^{C8} on chromatin. We tested DNA binding in solution using a 24bp double stranded
227 DNA probe and found that CBX8 is necessary for the DNA-binding activity of PRC1^{C8} (Fig. 3c).
228 Hence, CBX8 binding to DNA provides a second interaction site of PRC1 with chromatin.

229 We conclude that PRC1 interacts with chromatin via at least three distinct sites: PRC1^{C8}
230 binds to DNA and the H3 tail via CBX8, as shown herein (Fig. 3), and binds the nucleosome
231 acidic patch via RING1b-BMI1 as shown elsewhere³⁶. These multivalent interactions would
232 have to change dynamically while PRC1 maintains the condensed state of chromatin and
233 diffuses through it at the same time (Fig. 2b). Collectively, we propose that PRC1 induces
234 chromatin condensation via phase separation, through dynamic multivalent interactions
235 between PRC1 and chromatin.

236 **DNA binding by the CBX8 IDRs is required for efficient phase separation**

237 To test how different PRC1^{C8}-chromatin interaction sites affect phase separation, we
238 generated several different chromatin and CBX8 mutants (Fig. 4a and Extended Data Fig. 9).
239 Removing the CBX8 chromodomain (PRC1^{C8ΔChromo}), which interacts with the H3 tail^{37,38} (Fig.
240 3b), does not have a significant effect on phase separation (Fig. 4b,c). We then mutated 21
241 positively charged residues in the CBX8 IDRs to alanine (PRC1^{C8KR21A}). PRC1^{C8KR21A} is
242 analogous to a phase separation-deficient CBX2 mutant that was previously studied¹⁰.
243 Accordingly, PRC1^{C8KR21A} shows a clear defect in phase separation activity (Fig. 4b,c).

244 To further dissect the mechanism, we tested the DNA binding activity of PRC1^{C8KR21A} and
245 PRC1^{C8ΔChromo} against a 24 bp double-strand DNA probe with a sequence from a polycomb-
246 target gene. Both mutants are defective in DNA binding (Fig 4d). Hence, while DNA binding
247 of the chromodomain was reported previously³⁷, our data now suggests that the IDRs of
248 CBX8 are also contributing to DNA binding. We hypothesise that electrostatic interactions
249 between the negatively charged DNA to positive charges in the IDR lead to charge screening,
250 which promotes phase separation of chromatin (Fig. 4e).

251 We next set to determine if the H2A acidic patch of the nucleosome affects PRC1^{C8}-
252 chromatin condensation. For that, we mutated residues in the H2A acidic patch that were
253 previously shown to interfere with the interaction between PRC1 and the nucleosome³⁶
254 (Extended Data Fig. 9). We observed a change in the condensate morphology (Extended
255 Data Fig. 9a): while PRC1^{C8}-chromatin condensates appear spherical, the condensates with
256 mutated acidic patch chromatin adapt elongated and branched structures (Extended Data
257 Fig. 9a; most apparent at lower PRC1^{C8} concentrations). The effects of the PRC1^{C8KR21A}
258 mutant and the acidic patch chromatin mutant are additive (Extended Data Fig. 9b),
259 suggesting that both interaction sites contribute to phase separation independently. The
260 PRC1^{C8ΔChromo} mutant does not substantially affect phase separation, regardless of the
261 chromatin used (Extended Data Fig. 9c). Overall, our data supports a model where PRC1^{C8}

262 uses its chromodomain and IDRs to bind DNA. Then, PRC1^{C8} condenses chromatin through
263 interactions between the IDRs and DNA and, independently, between PRC1 and the acidic
264 patch on the nucleosomes (Fig 4e).

265

266 **CBX8 binding sites on chromatin in mouse embryonic stem cells are accessible**

267 Given the porous structure of PRC1^{C8}-condensed chromatin in vitro (Fig. 1) and the dynamic
268 diffusion of PRC1^{C8} within condensates (Fig. 2b), we next wished to probe for the
269 accessibility of PRC1^{C8}-bound chromatin in cells. We carried out the Assay for Transposase
270 Accessible Chromatin (ATAC-seq) in differentiated mESC, combined with ChIP-seq for CBX8
271 and H3K27me3. We used differentiated mESC, because CBX8 is expressed at very low levels
272 in pluripotent mESC and is upregulated during retinoic acid-induced cell differentiation (23
273 and Fig. 5a). The DNA-loaded Tn5 used in ATAC-seq experiments forms a dimeric complex of
274 approximately 130 kDa with an estimated hydrodynamic radius³⁹ of 4.6 nm (based on PDB
275 code 1MUH⁴⁰). In agreement with the accessibility analysis *in vitro* (Fig. 1h), the majority of
276 CBX8 ChIP-seq peaks in cells overlapped with ATAC-seq peaks (Figure 5b), indicating they
277 are accessible to Tn5. This observation was persistent across the genome, where ATAC-seq
278 peaks are co-localised with CBX8 and H3K27me3 peaks (Fig. 5c), indicating that CBX8-target
279 genes are largely accessible. The insufficiency of CBX8 to restrict chromatin accessibility is
280 further supported by the similar ATAC-seq profiles of wildtype and *Cbx8* knockout mESCs
281 (Fig. 5c,f, compare blue to orange). Hence, although the overall chromatin accessibility is
282 reduced during mESC differentiation (Fig. 5d,e), in agreement with previous works,⁴¹ this
283 process is not dependent on CBX8. Collectively, we show that CBX8-bound polycomb-
284 repressed chromatin is largely accessible in differentiated mESCs (Fig. 5b-f).

285 Data thus far suggest that the deletion of CBX8 does not change chromatin accessibility in
286 mESCs (Fig. 5c,f). Yet, other CBX proteins could potentially compensate for the loss of CBX8
287 in endogenous polycomb target genes. Therefore, we wished to test CBX8 in a system
288 where its recruitment is sufficient to trigger gene repression. To this end, we used a mESC
289 line that expresses a TetR-CBX8 fusion and includes a GFP reporter cassette downstream of
290 a TetO DNA binding array, stably integrated at chromosome 15 (coordinates: mm10 chr15:
291 79,013,675; Fig. 5g)⁴². In the absence of doxycycline (Dox), the TetR-CBX8 fusion is recruited
292 to the TetO-GFP reporter together with RING1B and initiates transcriptional repression (Fig.
293 5g and Extended Data Fig. 10a). However, GFP repression is reversible upon Dox addition,
294 which causes release of both TetR-CBX8 and RING1B from the TetO DNA binding array (Fig.
295 5g and Extended Data Fig. 10a).

296 Remarkably, ATAC-seq after prolonged Dox treatment did not reveal a substantial increase
297 in chromatin accessibility over the promoter region (Fig 5h). Small changes in the ATAC-seq
298 signal can be measured across samples and replicates, but these follow the sample-to-

299 sample variations globally (see Extended Data Fig. 10b for ATAC-seq coverage over the HoxA
300 genes cluster) and are therefore unlikely to be indicative of increased local accessibility.

301 The only increment in accessibility upon Dox treatment occurred downstream of the GFP
302 cassette, at a considerable distance from the TetO recruitment site and its adjacent PGK
303 reporter (Fig. 5h). That distal site includes another PGK promoter that is placed over 5 kbp
304 downstream to the TetO array. That distal PGK promoter originated from the construct that
305 was used to generate the reporter (⁴² and references therein) and does not express a
306 functional protein-coding mRNA. Hence, we cannot exclude the possibility that CBX8 affects
307 accessibility at sites distant from the main recruitment hub, possibly through indirect
308 effects. Nevertheless, the data indicate that CBX8 recruitment and subsequent gene
309 repression are insufficient to restrict chromatin accessibility at the recruitment site.

310 **Discussion**

311 In conclusion, we have shown that PRC1-CBX8 binds chromatin via multivalent interactions
312 and induces chromatin condensation using both the nucleosome interacting surface of PRC1
313 and the IDRs of CBX8. PRC1^{C8} is dynamic within condensates while keeping chromatin in a
314 static, solid-like state (Fig 3). This is in contrast to the liquid-like state of chromatin
315 condensates that were observed *in vitro*, in the absence of PRC1¹⁷. We established that
316 PRC1^{C8} is sufficient to induce the solid condensed state of chromatin.

317 How can PRC1 condense chromatin but yet maintain a highly dynamic behaviour in the
318 nucleus? PRC1 is characterised with a short residence time on chromatin³¹. Solid-like
319 chromatin that is condensed by a mobile chromatin binder has been shown *in vitro* for a
320 truncation of the SAM-domain protein Polyhomeotic (Ph)⁴³ and in cells for HP1a at
321 chromocenters²⁰. Yet, the mechanism allowing PRC1 and other gene-repressing factors to
322 condense chromatin while constantly diffusing in it remained largely unknown.

323 Our cryo-EM structure of PRC1-condensed chromatin explains how PRC1 can move in
324 condensed chromatin (Fig. 1), owing to the large pores that are formed between condensed
325 nucleosomes. The multivalent interactions between PRC1-CBX8 to chromatin provide PRC1
326 with multiple docking sites on chromatin: unmodified and modified H3 tail (Fig 3b-d), DNA
327 (Fig 3c) and the acidic patch of the nucleosome³⁶. Hence, it is possible that PRC1-CBX8 can
328 constantly change its interactions with chromatin to maintain its condensed structure while
329 utilising its different chromatin-interacting surfaces to dynamically move around. While
330 doing so, the positively charged IDRs of CBX8 mask the negative charge of the DNA to bring
331 together chromatin segments and stabilize the condensed state of chromatin (Fig. 5i).
332 Neither the DNA binding activity of the chromo domain (Fig. 4b) nor H3K27me3 (Fig. 3d)
333 seem to be necessary for efficient PRC1^{C8}-chromatin phase separation. A potential limitation
334 in the usage of a methyl-lysine analogue (Fig 3d) is that it may not always serve as a perfect
335 histone mimic (discussed in ³⁷). However, since the chromodomain of CBX8 is dispensable

336 for chromatin condensation (Fig. 4), it is plausible that histone tail binding may be
337 dispensable too. Given that the chromodomain is required for DNA binding (Fig. 4d) and
338 implicated in binding to H3K27me3^{37,38}, it may play a role predominantly in recruitment.

339 In cells, canonical PRC1 includes an additional PHC protein, which was previously implicated
340 in chromatin compaction and condensation^{8,28,43}. We reasoned that an in vitro study of a
341 simplified three-subunit complex, devoid of a PHC subunit, would allow us to characterize
342 the chromatin condensation activity of the CBX subunit. This minimal complex also allowed
343 us to overcome difficulties in purifying a PHC-bound PRC1 complex in sufficient quantities
344 and purity for structural studies. It is plausible that the chromatin compaction activities of
345 CBX8 and the PHC subunit cooperate in vivo and the absence of a PHC subunit in our
346 experiments presents a limitation when trying to extrapolate from our in vitro results.

347 While our experiments were not designed to extensively characterise the contribution of
348 protein-protein interactions towards phase separation or chromatin condensation, we
349 cannot exclude their involvement. Indeed, oligomerization of BMI1 was reported⁴⁴ and PHC
350 polymerization influences PRC1-chromatin condensate properties²⁸. However, PRC1^{C8} does
351 not form condensates in the absence of chromatin in vitro (Fig 1e). Furthermore, there are
352 only about 10 PRC1 molecules per polycomb domain in cells³¹, which is a factor that needs
353 to be considered when attempting to link protein oligomerization to chromatin compaction.
354 More studies are needed to determine how PRC1 molecules are distributed and work
355 together within polycomb domains in vivo and how protein-protein and protein-DNA
356 interactions contribute to this process.

357 Our data indicate that chromatin condensation together with dynamic behaviour within
358 chromatin condensates is an intrinsic biophysical property of PRC1-CBX8. It is plausible that
359 the dynamic behaviour of PRC1 within chromatin condensates is required in order to allow
360 PRC1 to modify nucleosomes by the H2AK119ub mark while holding them together. This
361 phenomenon might represent a broad paradigm of repressive chromatin. The internal
362 structure of PRC1-chromatin condensates is a porous network of nucleosomes (Fig. 1). Such
363 a structure could present a size-selective diffusion barrier, in agreement with its
364 permeability to PRC1 diffusion in vitro (Fig. 2) and Tn5 accessibility in cells (Fig. 5). The
365 existence of such a size-selective diffusion barrier remains to be identified in vivo, where it
366 may contribute to gene repression by selectively excluding transcriptional coactivators,
367 which are commonly large protein complexes- (>1MDa^{12,45-47}). ATAC-seq experiments reach
368 their limitations in this context, because of the small size of the Tn5 used in these assays.
369 Hence, from our experiments in cells, we can only conclude that CBX8-bound chromatin is
370 not entirely inaccessible. Future studies may develop size-selective probes to directly
371 address questions of size-selective chromatin accessibility genome-wide. The hypothesis
372 that polycomb-mediated repression antagonises Pol II transcription without blocking all
373 proteins has been made nearly three decades ago⁴⁸. This idea was conceived based on the
374 observation that T7 polymerase (~100 kDa) can initiate transcription from a polycomb-

375 repressed locus but GAL4-dependent transcriptional activation does not take place there.
376 This is in agreement with the inverse correlation between the density of chromatin domains
377 and the molecular weight of the chromatin modifiers present in them¹². Transcription factor
378 size has also been suggested to determine access to different chromatin domains based on
379 simulations⁴⁹. Combining our results with earlier findings^{12,19,20,49}, we propose that size-
380 selective exclusion may be part of a broader mechanism by which chromatin-interacting
381 proteins regulate the accessibility of repressive chromatin.

382 **Acknowledgements:** We would like to thank the Ramaciotti centre for electron microscopy
383 at Monash university for providing instrumentation, technical support and collecting cryo-ET
384 data, the Monash Proteomics facility for providing instrumentation and technical support
385 and the Monash Micro Imaging facility for providing instrumentation and technical support.
386 We would also like to acknowledge the MASSIVE HPC platform for providing high-
387 performance computing resources

388

389 **Funding:** This work was supported by an Australian research council (ARC) DECRA fellowship
390 DE210101669 (M.U.), NIH-NIMH R01MH122565 (O.B.), start-up funding from the Norris
391 Comprehensive Cancer Center at Keck School of Medicine of USC (O.B.), NIH-T32 training
392 grant T32HD060549 (J.M.), Sylvia and Charles Viertel Senior Medical Research Fellowship
393 (C.D.) and the National Health and Medical Research Council (NHMRC) grant numbers
394 APP1162921, APP1184637 and APP2011767 (C.D.). C.D. is an EMBL-Australia Group Leader.

395

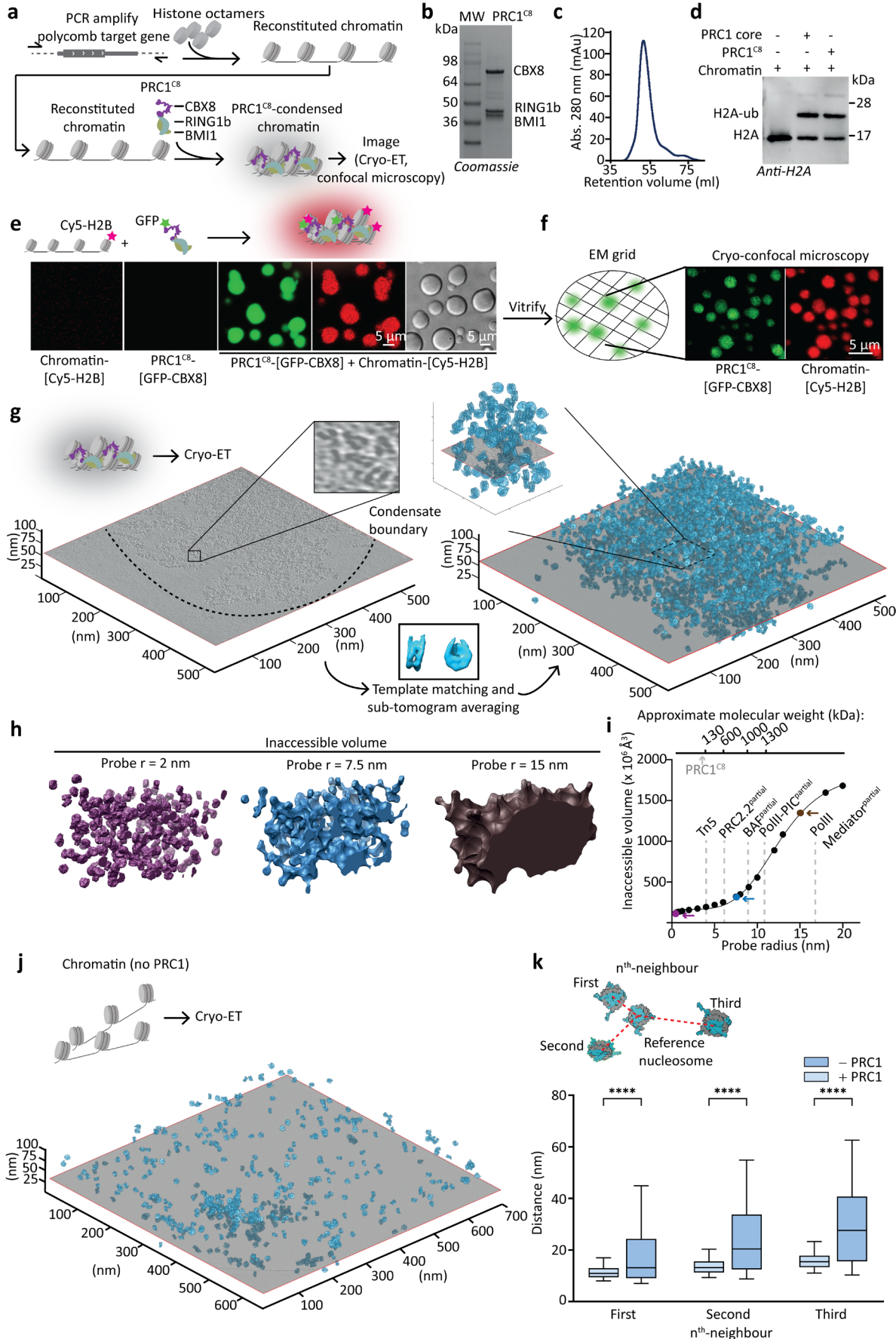
396 **Authors contributions:** C.D. and M.U. conceptualised the project and acquired funding,
397 M.U., V.L., C.T., X.H.N., J.M., J.H., S.M., H.V., S.T., M.B. and M.L. carried out experiments and
398 investigated, P.P.D. and V.P. generated cell lines, S.F. and Q.Z. cloned and purified histone
399 mutants, M.L. and M.U. developed software, C.D., A.d.M., O.B., P.P.D., Y.G. and E.G.
400 supervised, M.U. and C.D. wrote the original draft and all authors reviewed and edited the
401 manuscript.

402

403 **Declaration of interests:** The authors declare no conflict of interest.

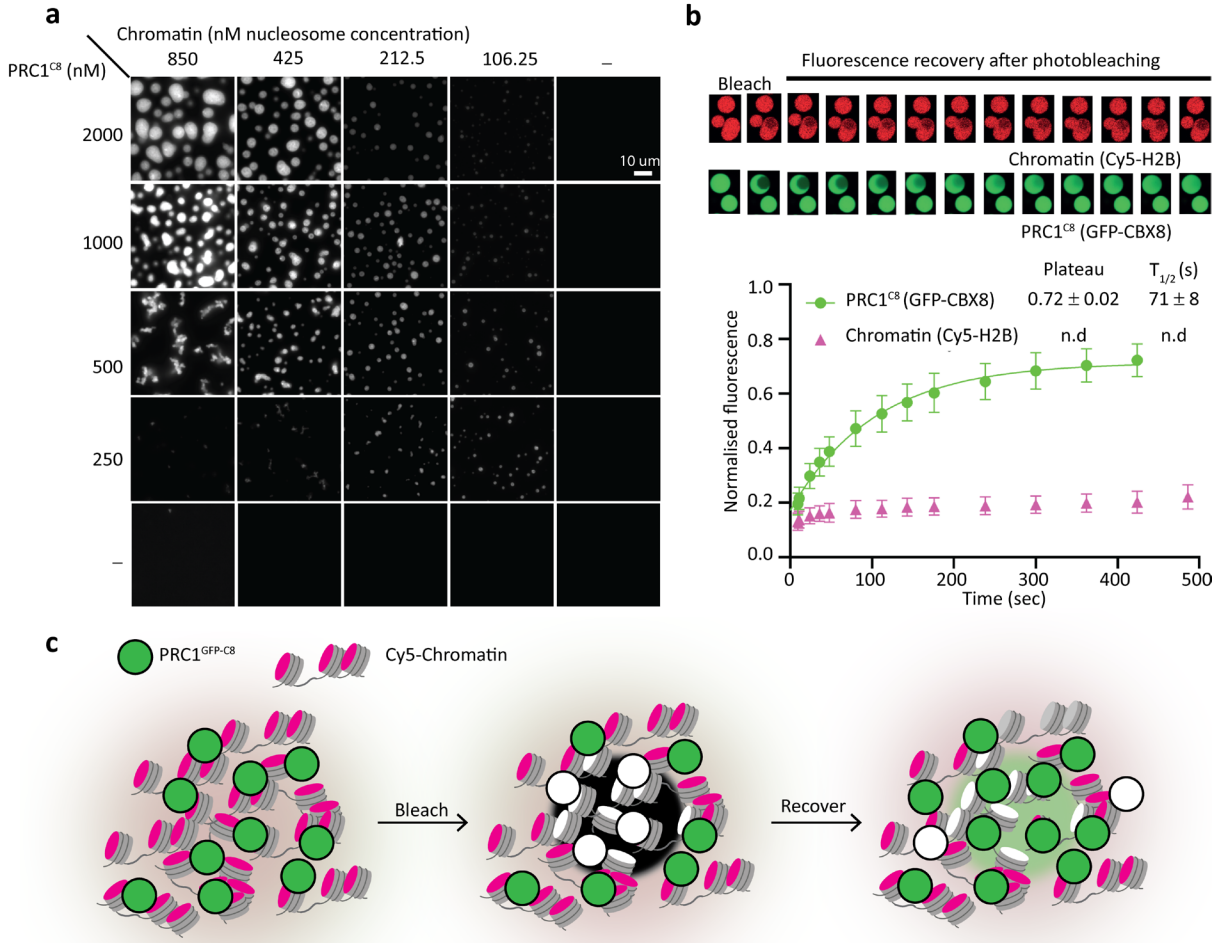
404

405 **Data and materials availability:** Next generation sequencing data (ATAC-seq and ChIP-seq)
406 are available under GEO accession number GSE220140. The maps for tomograms in Fig. 1 g,
407 and j have been deposited to the EMD (EMD-29022 and EMD-43554, respectively). All cryo-
408 ET raw data has been deposited to EMPIAR under accession numbers EMPIAR-11344 and
409 EMPIAR-11883, of chromatin in the presence and absence of PRC1-CBX8, respectively. XL-
410 MS data has been deposited to Pride (PXD039589 and PXD049094).



413 **Fig. 1. The molecular structure of PRC1-chromatin condensates is porous and accessible to**
414 **macromolecules.** **a**, Schematics introducing the workflow. **b**, SDS-PAGE of purified PRC1^{C8}
415 complex that includes RING1b, BMI1 and MBP-tagged CBX8. **c**, Size exclusion
416 chromatography of the purified PRC1^{C8} using a HiLoad Sephadryl 300 16/60 column. **d**, In
417 vitro ubiquitylation assay comparing PRC1^{C8} to a RING1b-BMI1 heterodimer. Samples in
418 lane 2 and 3 included E1, E2, ubiquitin and ATP. Ubiquitylation is detected by western blot
419 using an anti-H2A antibody. **e**, Chromatin condensates induced by the PRC1^{C8} complex and
420 the individual proteins, visualised by confocal (left and centre) and phase contrast (right,
421 from independent experiments) microscopy. CBX8 is GFP-labelled and chromatin is Cy5
422 labelled. Protein and chromatin concentrations are 1 μ M and 20 nM (estimated nucleosome
423 concentration), respectively. **f**, Cryo-confocal microscopy of vitrified PRC1^{C8}-chromatin
424 condensates. **g**, Cryo-electron tomography of a PRC1^{C8}-chromatin condensate. Shown is a
425 central slice through the reconstruction (left image). Nucleosome subtomogram averages
426 (centre, bottom) are then placed in a volume the size of the tomographic slice, at the
427 position and orientation determined by template matching and subtomogram averaging
428 (right image). 1330 nM PRC1^{C8} and 3500 nM chromatin (estimated nucleosome
429 concentration) were assayed in 3.5 mM HEPES-KOH pH 7.5, 6.8 mM TRIS-HCl PH 7.5, 21 mM
430 NaCl, 7 mM KCl, 0.8 mM DTT. See Supplementary Data 1 for a list of cross correlation peaks.
431 **h**, Surface representation of the volume of a subset of the PRC1^{C8}-chromatin condensate
432 structure that is inaccessible to probes of given radii. **i**, Inaccessible volumes for a given
433 probe radii are plotted, with exemplary molecules indicated (in grey) and selected probes
434 coloured as in **h**. For the indicated complexes, the hydrodynamic radius was estimated³²
435 using resolved domains from published structures (see Methods section for PDB accessions)
436 as a minimum size estimate. **j**, As in **g** but without PRC1^{C8}. See Supplementary Data 2 for a
437 list of cross correlation peaks. **k**, Pairwise distances of each individual nucleosome to its
438 nearest three neighbouring nucleosomes in 3D space in tomograms with and without
439 PRC1^{C8}. Only unique pairs are plotted from two tomograms with (+PRC1) and three
440 tomograms without (-PRC1). Whiskers extend from the 5th to the 95th percentiles.
441 Significance was tested using a Brown-Forsythe ANOVA with a Games-Howell post hoc test.
442 *** = p-value < 0.0001.

443

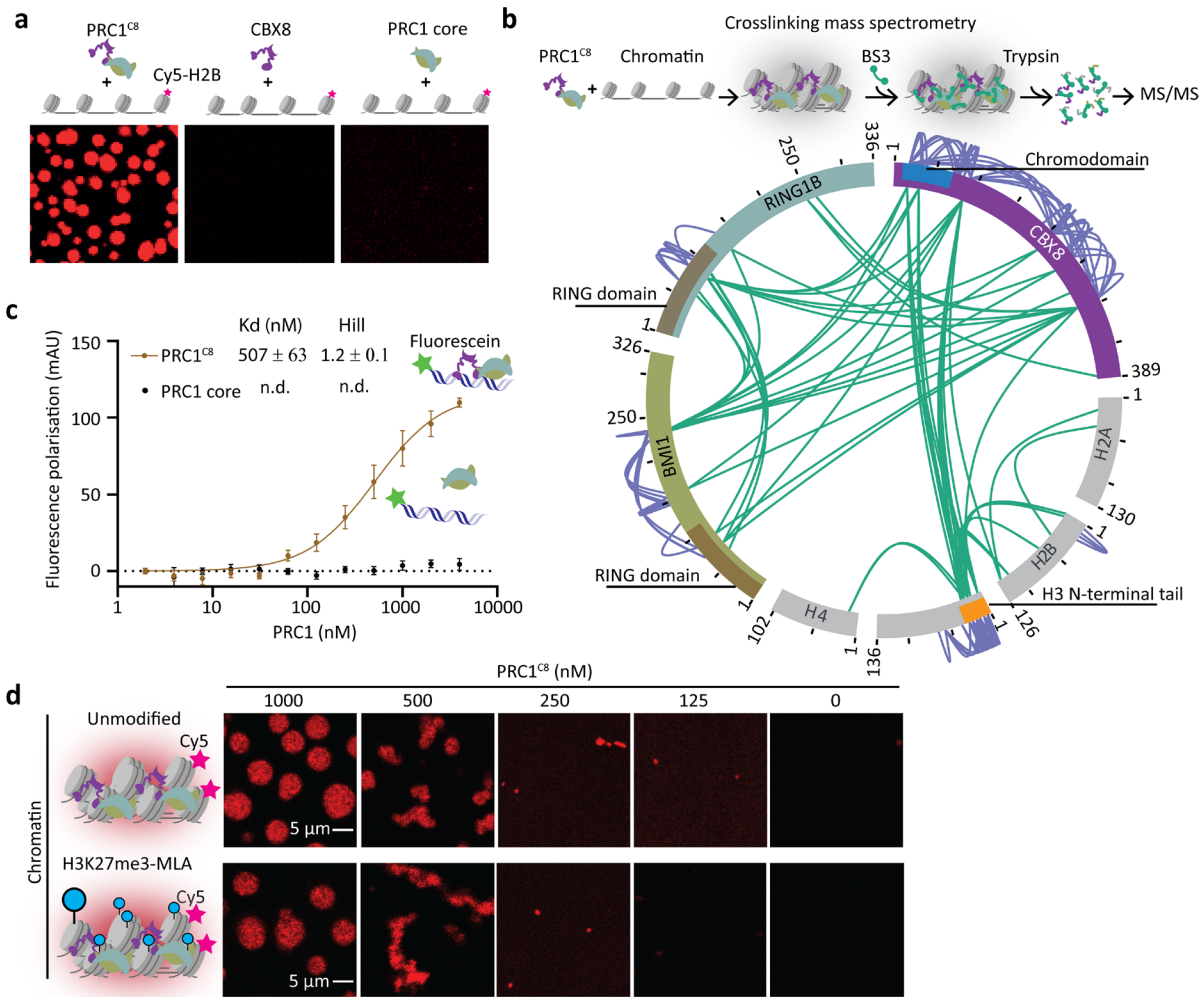


444

445 **Fig. 2. PRC1^{C8} is mobile while chromatin is static within PRC1-chromatin condensates.**

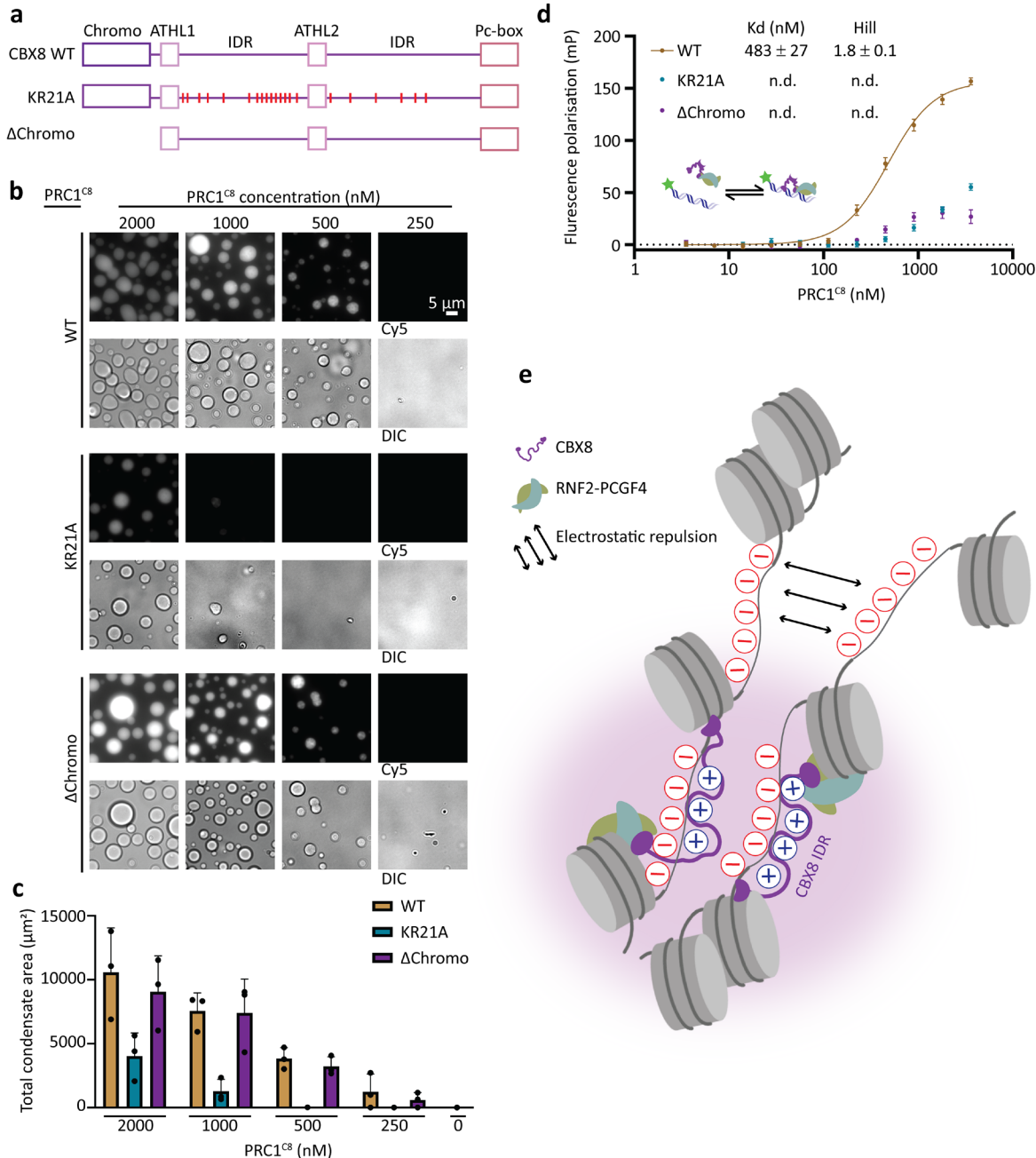
446 **a**, Titration of Chromatin against PRC1^{C8}. Condensates were assessed with a fluorescence
447 widefield microscope imaging a Cy5 label on the chromatin. Presented are representative
448 micrographs of three replicates, including two with MBP-tagged PRC1^{C8} (presented) and one
449 with GFP-tagged PRC1^{C8}. **b**, Representative micrographs of FRAP recorded in PRC1^{C8}-
450 chromatin condensates. CBX8 is GFP labelled and chromatin is Cy5 labelled. Mean
451 fluorescence intensity of the bleached area, normalised to pre-bleach mean signal, is plotted
452 for every time point. Error bars show standard deviation from n=7 (GFP) and n=8 (Cy5)
453 measurements recorded from two independent experiments. The GFP signal recovery was
454 fit with an exponential association model, best fit values for Plateau and fluorescence
455 recovery half time ($T_{1/2}$) are shown with standard error. **c**, Schematic representation of the
456 FRAP experiment.

457



458
459 **Fig. 3. Multivalent interactions between PRC1^{C8} and chromatin. a**, Chromatin condensation
460 in response to the whole PRC1^{C8} complex (RING1b, BMI1 and CBX8) or the individual
461 components CBX8 and the RING1b–BMI1 heterodimer. Representative images from two
462 replicates. **b**, Intramolecular (purple lines) and intermolecular (green lines) protein-protein
463 interactions mapped within PRC1-chromatin condensates using crosslinking mass
464 spectrometry (XL-MS). Data is from three independent replicates. **c**, PRC1^{C8} or PRC1 core
465 binding to a fluorescein labelled 24bp DNA probe measured by fluorescence polarisation.
466 Data points show the mean (baseline subtracted) of three independent replicates and the
467 error bars indicate the standard error. The continuous line represents the fit to a Hill binding
468 model, when applicable. **d**, Titration of PRC1^{C8} to unmodified chromatin (top) and
469 H3K27me3-MLA chromatin (bottom) at an identical chromatin concentration (50 ng/μl DNA)
470 and 150 mM KCl. Micrographs are representative of two independent replicates.

471

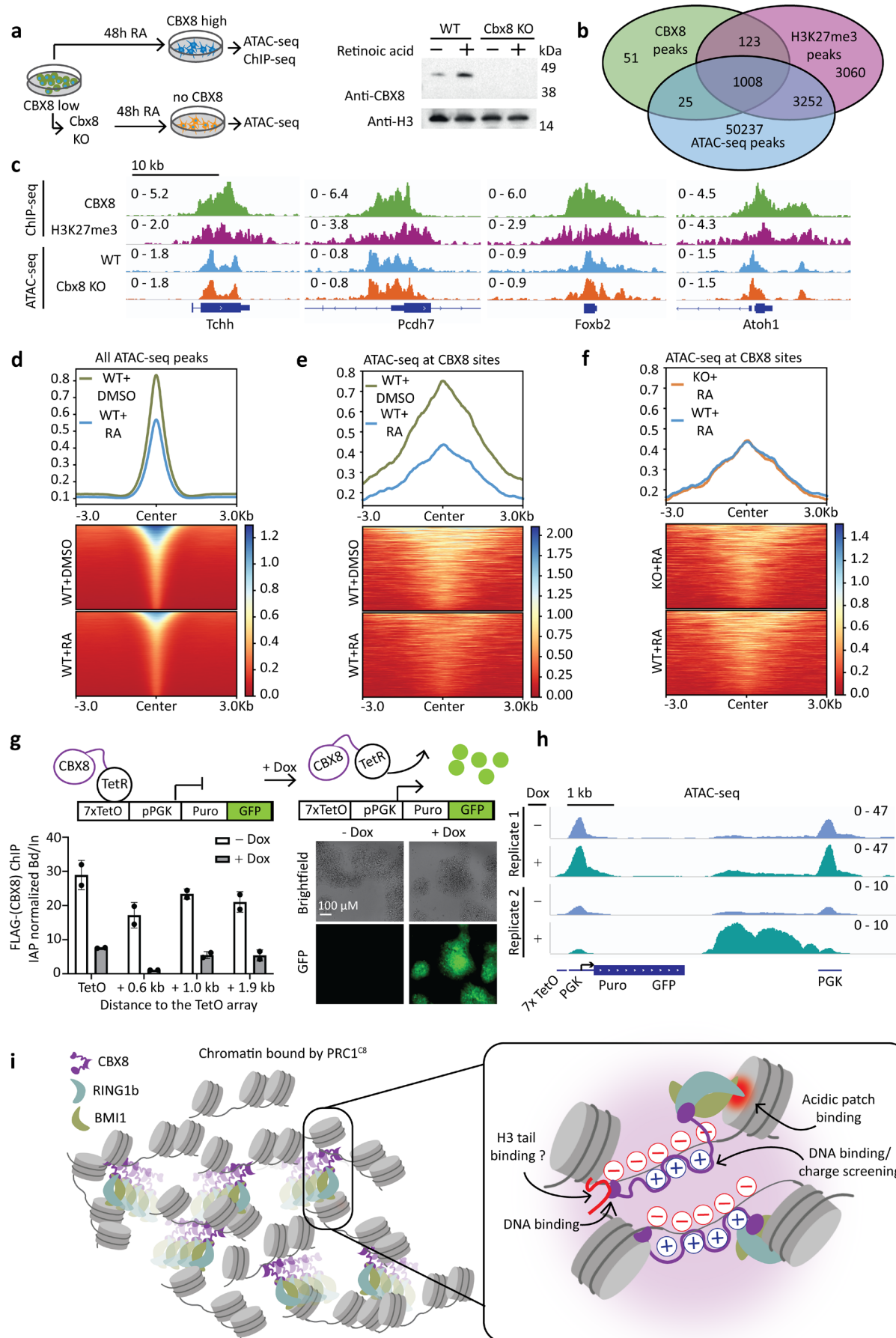


472

473 **Fig. 4. Positive charges in the CBX8 IDRs are required for DNA binding and phase**
474 **separation.** **a**, Schematics depicting the different CBX8 mutants used, drawn to scale. **b**,

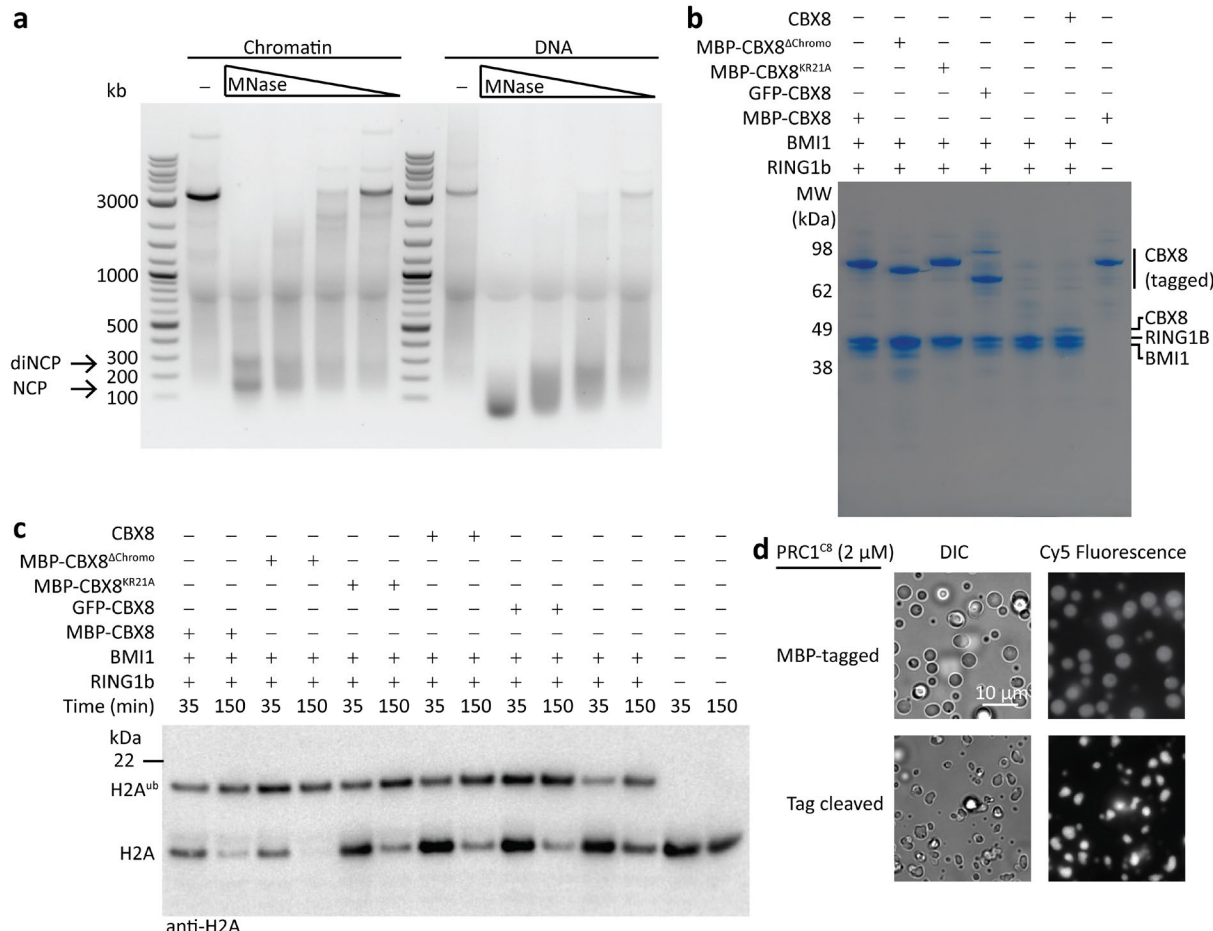
475 PRC1^{C8}-chromatin condensates in the context of different CBX8 mutants. Varying
476 concentrations of PRC1^{C8} were titrated to a constant concentration of C5-labelled
477 reconstituted chromatin (50 ng/ μ l). Widefield fluorescence and differential interference
478 contrast (DIC) micrographs are representative of three replicates. **c** Quantification of the
479 total area covered by condensates per micrograph for different PRC1^{C8} mutants and
480 concentrations. Bars represent the means from three independent replicates and error bars
481 represent the standard deviation. **d**, Fluorescence polarisation assay measured the affinity
482 of different PRC1^{C8} mutants for a Fluorescein-labelled 24 bp DNA probe. Data points are the
483 mean (baseline subtracted) of three independent replicates and error bars indicate the

484 standard error. The continuous line represents the fit to a Hill binding model, when
485 applicable. **e**, Model for chromatin condensation by PRC1^{C8}: Electrostatic interaction
486 between the CBX8 IDR with DNA provides charge screening and promotes phase separation.



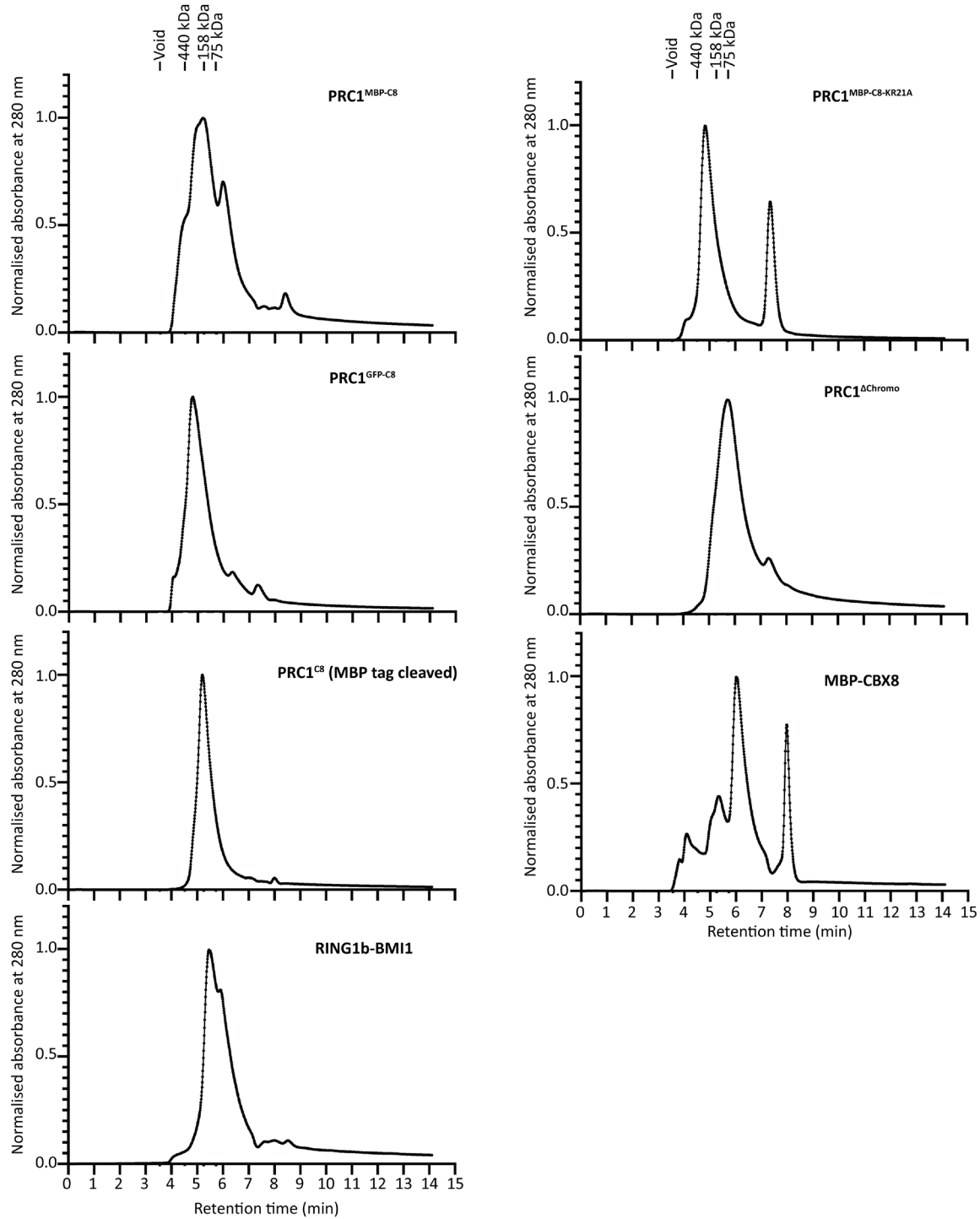
488 **Fig. 5. CBX8 binding sites on chromatin in mouse embryonic stem cells are accessible.**
489 **a**, Schematics of the experimental setup (left) and anti-CBX8 western blot (right) of wildtype
490 and *Cbx8* knockout mESC after 48 hours of retinoic acid (RA) treatment. **b**, Overlap of ATAC-
491 seq peaks and CBX8 and H3K27me3 ChIP-seq peaks. ATAC-seq peaks are defined from two
492 biological replicates. **c**, ChIP-seq traces for H3K27me3 and CBX8 in wildtype mESC and
493 representative ATAC-seq traces at four genes in wildtype and CBX8 knockout mESC after 48
494 hours of RA treatment. **d**, Accessibility changes at all ATAC-seq peaks in wildtype (WT)
495 mESC, in response to retinoic acid (RA) treatment. **e**, Accessibility changes at all CBX8-target
496 sites in wildtype mESC, in response to RA treatment. **f**, Comparison of accessibility at CBX8-
497 target sites between wildtype and *Cbx8* knockout cells after RA treatment. **g**, Top: schematic
498 representation of the chromosome-integrated reporter. Left panel: ChIP-qPCR using FLAG
499 antibody (CBX8 is FLAG tagged) at indicated distances from the TetO array, in the presence
500 and absence of doxycycline (Dox) treatment for six hours. Bars represent the mean bound
501 over input (Bd/In) normalised to the IAP gene and points represent two replicates. See
502 Extended Data Fig 10a for ChIP-qPCR using additional antibodies. Right panel: Brightfield
503 and GFP-fluorescence images of the mECS cells before and after Dox treatment. **h**, ATAC-seq
504 signal reporting accessibility of the integrated locus before and after Dox treatment for six
505 days. From left to right: annotated are the TetO array and its proximal PGK promoter that
506 controls the Puromycin-GFP reporter gene, and the distal PGK promoter. **i**, Model: PRC1
507 forms multivalent interactions with chromatin, thereby stabilizing chromatin condensates
508 potentially through charge screening of negatively charged DNA by positive charges in the
509 CBX8 IDR. These interactions dynamically change as PRC1 diffuses through condensates.
510

511 **Extended Data**



512
513

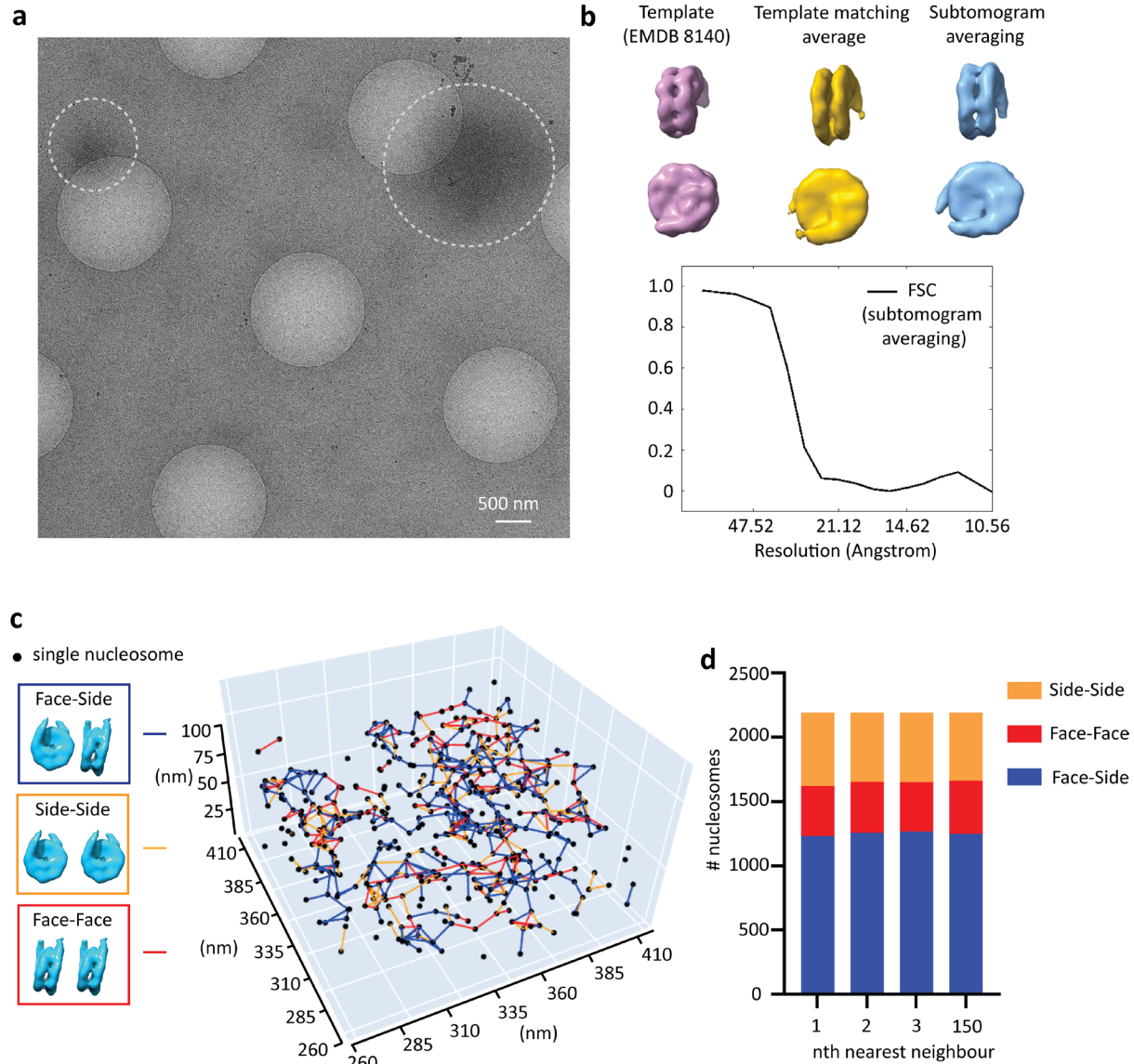
514 **Extended Data Fig. 1. Quality control of chromatin and protein constructs. a, MNase**
 515 digestion of reconstituted Chromatin and a naked DNA (same sequence as used for
 516 chromatin reconstitution). DNA fragments post digestion are resolved on a 1.2 % Agarose
 517 gel. Protected bands indicating mono- and di-nucleosome core particles (NCP and diNCP)
 518 are indicated by the arrows. **b, 3 ug of each protein complex used in this study resolved on a**
 519 **4-12% SDS-PAGE gel stained with Coomassie. c, Ubiquitylation activity of each protein**
 520 **complex used in this study visualized on a western blot. All samples include UBA1, UBCH5C,**
 521 **Ubiquitin, ATP and 1 uM chromatin (nucleosome concentration). d, Phase separation**
 522 **experiment comparing chromatin condensation activity of PRC1^{C8} with MBP-tagged CBX8 to**
 523 **PRC1^{C8} with the tag cleaved.**



524

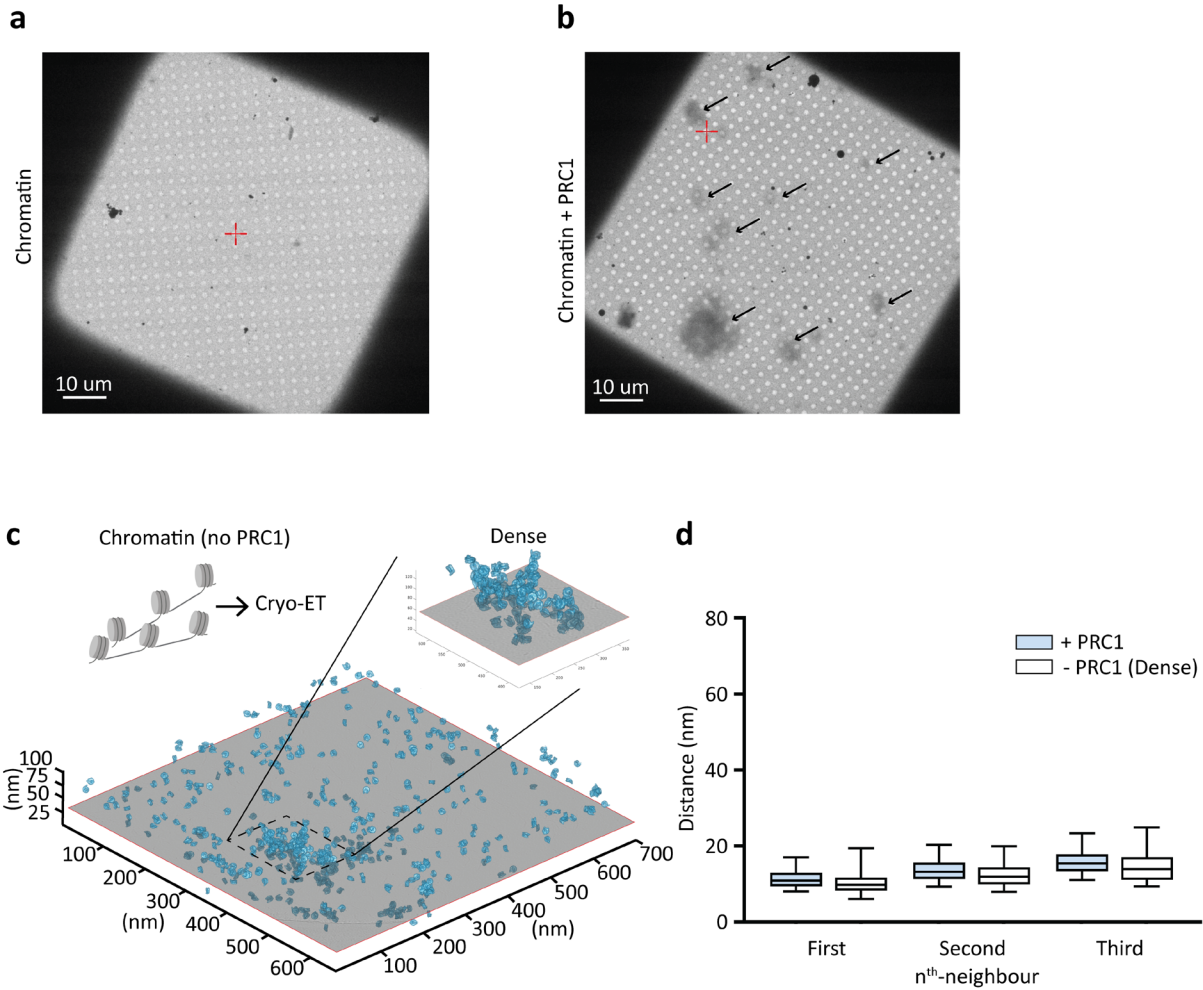
525 **Extended Data Fig. 2. PRC1 complexes used in this study are monodispersed.** HPLC elution
526 profiles from a Shim-pack Bio Diol 200 HPLC column for each of the purified protein
527 complexes, as indicated.

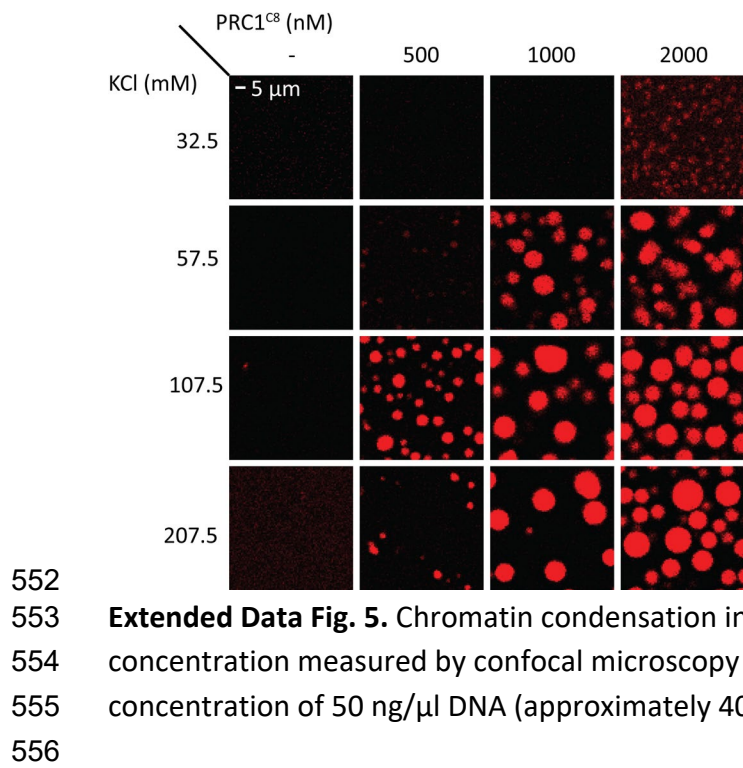
528



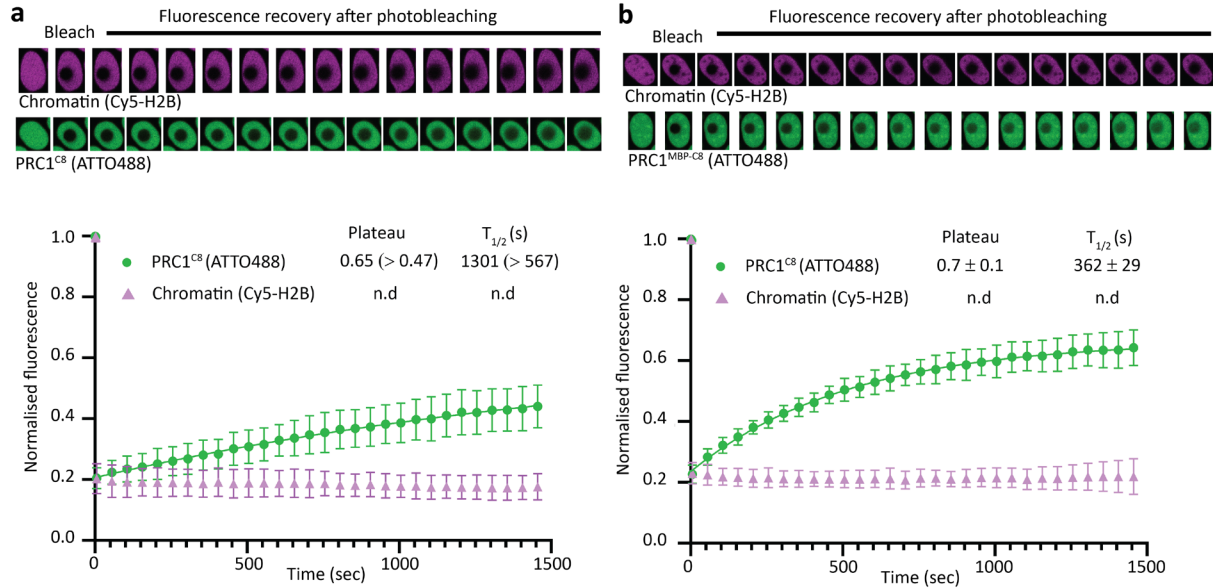
529

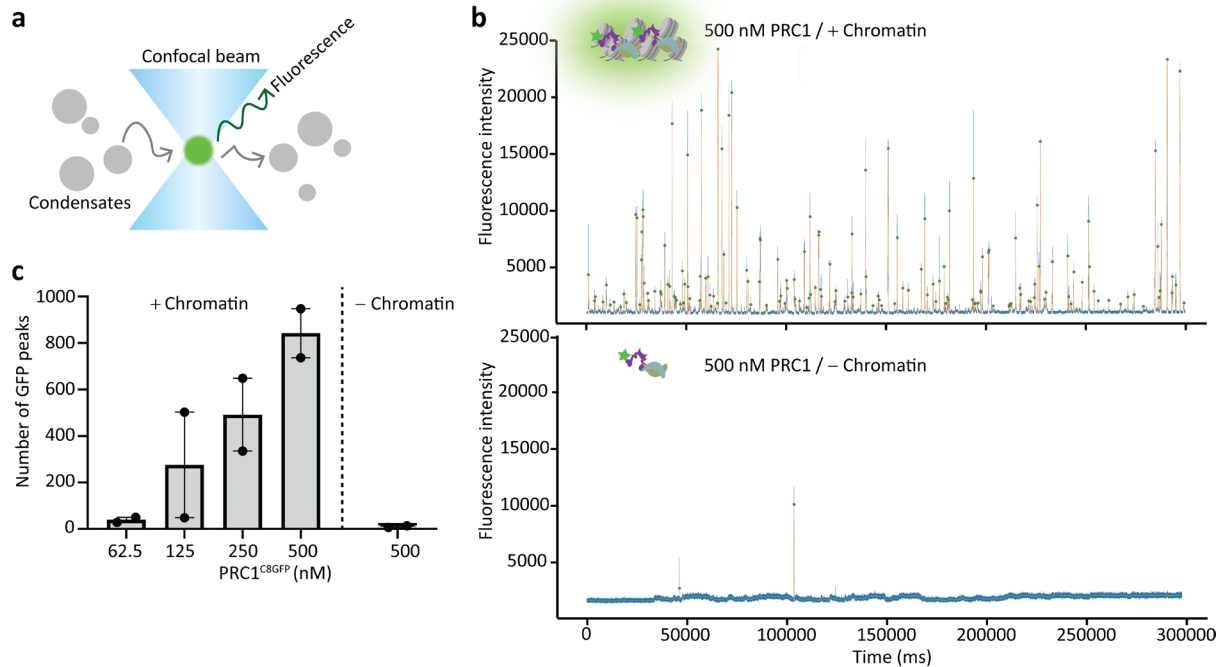
530 **Extended Data Fig. 3. Nucleosomes in PRC1^{C8}-chromatin condensates show no orientation**
531 **bias towards neighbouring nucleosomes.** **a**, Low-magnification micrograph showing
532 examples of dense regions suspected to be condensates (dashed circles). Tomograms were
533 collected at the borders of regions such as these. Micrographs are from the same grid from
534 which tomograms were collected. **b**, Structures of the template used for template matching
535 (left), the averaged structure after template matching (middle) and the final structure after
536 the subtomogram averaging routine (right) with the related Fourier shell correlation curve
537 (bottom). **c**, Orientations of nucleosomes towards neighbouring nucleosomes within a cut-
538 off of 20 nm. Individual points represent nucleosomes and lines between points are
539 coloured according to the relative orientation of neighbouring nucleosomes as indicated in
540 the colour key (left). **d**, Distribution of nucleosome-nucleosome orientation for the three
541 nearest neighbours and the 150th neighbour of each nucleosome in tomogram #1. Colours
542 correspond to the same respective orientations as in **c**.





553 **Extended Data Fig. 5.** Chromatin condensation in response to variations in salt and PRC1
554 concentration measured by confocal microscopy using Cy5-labelled chromatin at a constant
555 concentration of 50 ng/μl DNA (approximately 400 nM nucleosomes).
556

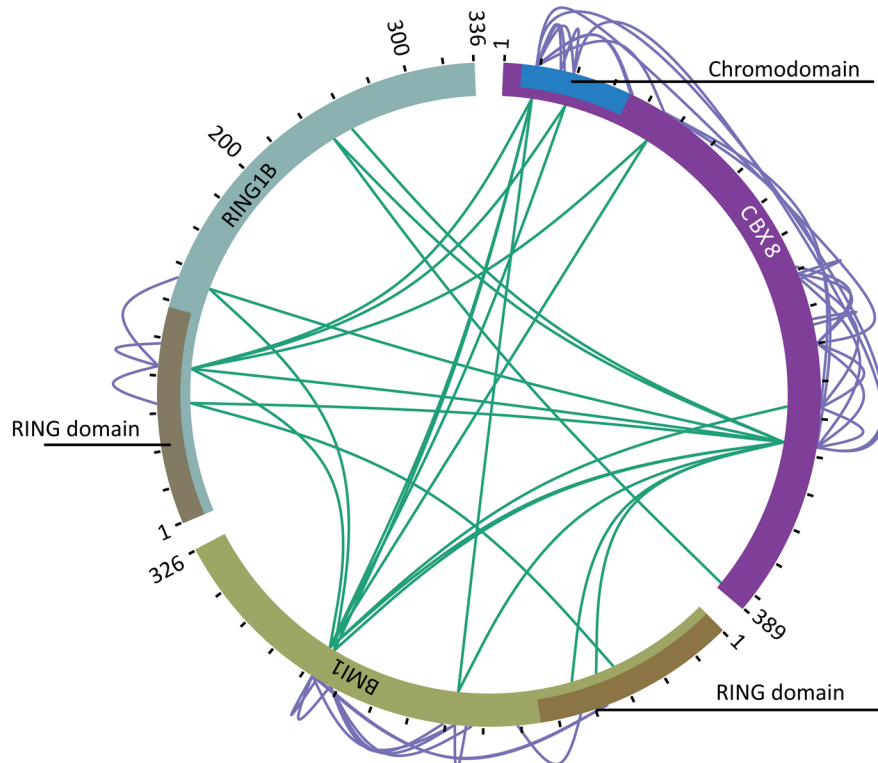




576

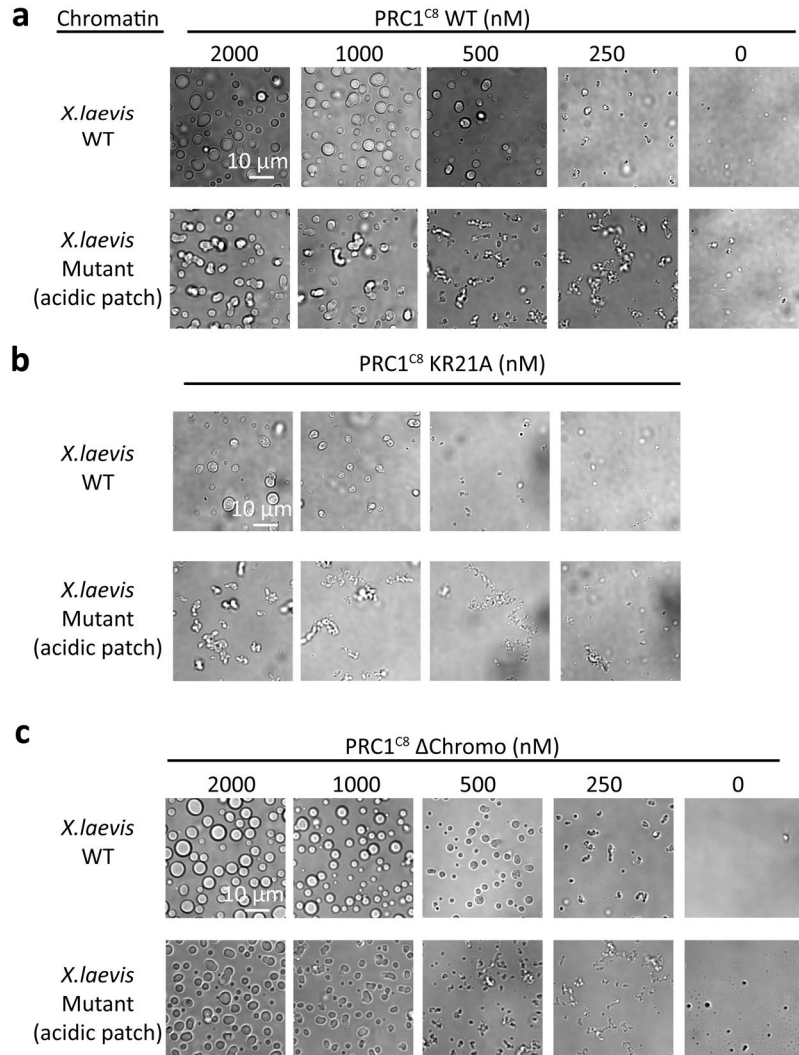
577 **Extended Data Fig. 7. Condensates can be detected at physiologically relevant PRC1^{C8}**
578 **concentrations. a,** An illustration of single molecule confocal microscopy. Individual
579 condensates (in grey) are detected when diffusing through the confocal volume (in blue)
580 and emitting GFP fluorescence (in green). **b,** Top: representative trace tracking GFP signal
581 over time for samples with 500 nM GFP-labelled PRC1^{C8} and chromatin (200 nM nucleosome
582 concentration). Traces show a 5 minute window from a 20 minute experiment. Blue lines
583 show the raw GFP signal and orange lines show the GFP signal after low-pass filtering using
584 a Butterworth filter. Green dots indicate the maxima of the detected peaks. Bottom: same
585 as the top plot, but in the absence of chromatin. **c,** GFP peak counts at different PRC1^{C8}
586 concentrations. Data from two replicates are shown. Bars indicate the mean of two
587 independent replicates that were carried out on different days, the error bars show the
588 standard error of the mean and individual data points are presented.

589



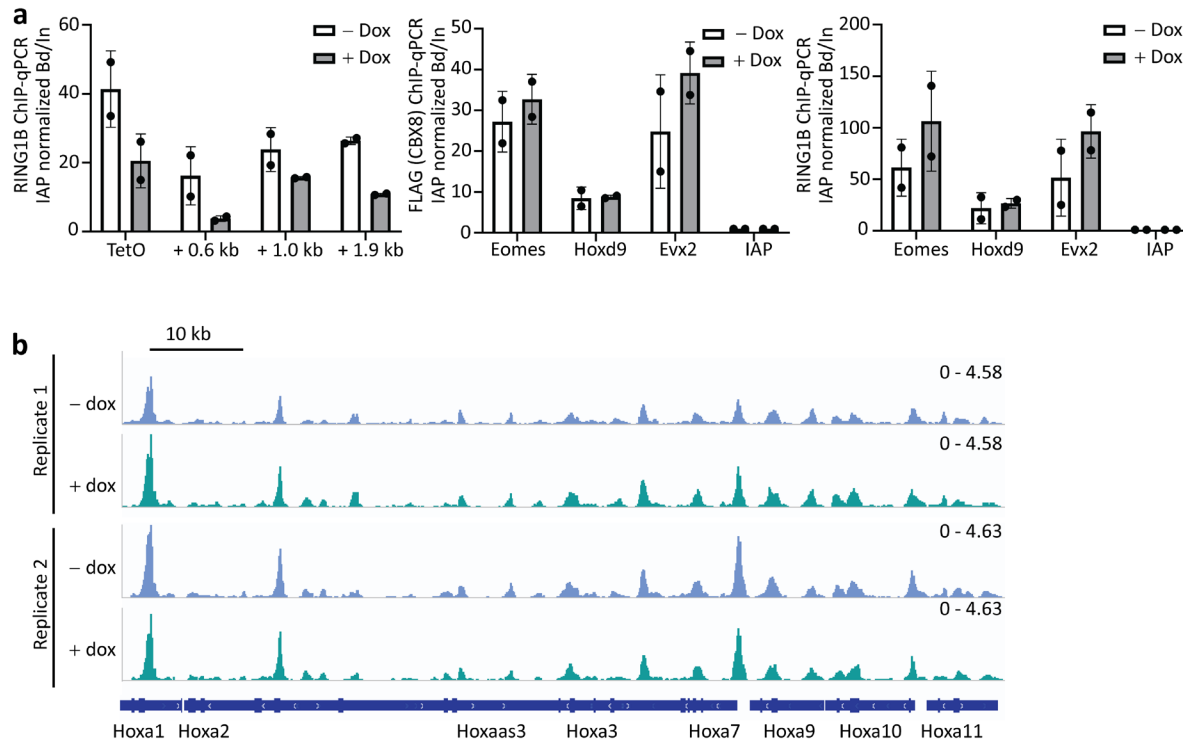
590
591
592
593

Extended Data Fig. 8. Crosslinking mass spectrometry (XL-MS) profile of PRC1^{C8} is similar in the absence of chromatin. Same experiment as in Fig. 3b, but without chromatin.



594 **Extended Data Fig. 9. The nucleosome acidic patch is required for efficient PRC1-
595 chromatin phase separation. a** Phase separation of *X. laevis* wildtype and acidic patch
596 mutant chromatin in response to increasing concentrations of PRC1^{C8} wildtype. DIC
597 micrographs are representative of two replicates. **b** Same as (a), but with the PRC1^{C8KR21A}
598 mutant. **c** Same as (a) but with the PRC1^{C8ΔChromo} mutant.

600



601 **Extended Data Fig. 10. a**, ChIP-qPCR in the presence and absence of doxycycline (Dox)
602 treatment using RING1B antibody at indicated distances from a chromosome-integrated
603 TetO array (left), at control genes (right) and using FLAG (CBX8) antibodies at control genes
604 (middle). Bars represented the bound over input (Bd/ln) normalised to the IAP gene and the
605 dots represent individual data points. **b**, ATAC-seq signal at the HoxA locus of the reporter-
606 integrated mECS cell line before and after dox treatment. Two independent replicates are
607 shown.

609 **Extended Data Movie S1. Related to Fig.1; Cryo-tomogram of a PRC1^{C8}-chromatin
610 condensate.** The movie shows a scan through the z-axis of denoised⁵⁰ tomogram of
611 chromatin in presence of PRC1.

612
613 **Extended Data Movie S2. Related to Fig.1; Cryo-tomogram of chromatin without PRC1.**
614 The movie shows a scan through the z-axis of denoised⁵⁰ tomogram of chromatin in absence
615 of PRC1.

616
617 **Supplemental Table 1. Template matching results for PRC1^{C8}-chromatin condensates.**
618 Results from the Dynamo template matching process before manually removing false
619 positive hits, in Excel format. Every entry describes a cross correlation peak above the cut-
620 off of 0.17. Each peak indicates the position of a nucleosome at x-y-z coordinates given in
621 columns 24-26 and at rotations applied to the template as defined by Euler angles in
622 columns 7-9. The table is also provided in Dynamo format (.tbl) for direct import into
623 Dynamo (Supplementary Data 1).

624
625 **Supplemental Table 2. Template matching results for chromatin without PRC1^{C8}.** Results
626 from the dynamo template matching process before manually removing false positive hits in
627 Excel format. Every entry describes a cross correlation peak above the cut-off of 0.23. Each
628 peak indicates the position of a nucleosome at x-y-z coordinates given in columns 24-26 and
629 at rotations applied to the template as defined by Euler angles in columns 7-9. The table is
630 also provided in Dynamo format (.tbl) for direct import into Dynamo.

631
632 **Supplementary Data 1. Template matching results for chromatin without PRC1^{C8}.** Same as
633 Supplemental Table 1, provided in Dynamo format (.tbl) for direct import into Dynamo.

634
635 **Supplementary Data 2. Template matching results for PRC1^{C8}-chromatin condensates.**
636 Same as Supplemental Table 3, provided in Dynamo format (.tbl) for direct import into
637 Dynamo.

638
639 **Supplementary Data 3. XL-MS-identified crosslinks within PRC1^{C8}.** Provided is a list of the
640 crosslinks that were detected using XL-MS within PRC1^{C8} in the absence of chromatin.

641 **Supplementary Data 4. XL-MS-identified crosslinks within PRC1^{C8}-chromatin.** Provided is a
642 list of the crosslinks that were detected using XL-MS within PRC1^{C8} in the presence of
643 chromatin.
644
645
646

647 **Materials and Methods**

648 **Plasmids and cloning**

649

650 Human RING1b (Uniprot ID Q99496) and human BMI1 (Uniprot ID P35226) were cloned into
651 a pFBOH-mhl vector (Addgene plasmid # 62304) cleaved with BseRI using Gibson Assembly®
652 Master Mix (NEB #E2611L) using the primers indicated in Table S1.

653 Human CBX8 wildtype open reading frame (Uniprot ID Q9HC52-1 and NCBI Reference
654 Sequence was NM_020649.2) was obtained from gene synthesis (Gen9). The CBX8^{KR21A}
655 mutant open reading frame was codon optimised for expression in *Trichoplusia ni* insect
656 cells and synthesised (Genscript). The CBX8^{ΔChromo} truncation was amplified from the
657 wildtype ORF using primers indicated in Table 1 and then subcloned into a vector with the
658 same backbone as used to express the wild type protein. All three CBX8 constructs were
659 cloned into a modified pFastBac1 pFB1.HMBP.A3.PrS.ybbR vector digested by Xhol and XmaI
660 sites to include a N-terminal 6xHis-MBP tag. Cloning of the polycomb target gene ATOH1
661 into the pUC18 vector was described previously⁵¹. Plasmids for expression of human
662 histones (H2A, H2B, H3.1 and H4) in *E.coli* were a kind gift from David Tremethick,
663 Australian National University. UbcH5c WT pET28a was a gift from Rachel Klevit (Addgene
664 plasmid # 12643; <http://n2t.net/addgene:12643>; RRID:Addgene_12643)⁵².

665 pET3a-hUBA1 was a gift from Titia Sixma (Addgene plasmid # 63571;

666 <http://n2t.net/addgene:63571>; RRID:Addgene_63571)⁵³.

667 To generate a baculovirus expression vector of a monomeric EGFP-CBX8 (mEGFP-CBX8)
668 construct, first GFP was amplified from a pSpCas9(BB)-2A-GFP vector and CBX8 was
669 amplified from a pFB1.HMBP.A3.PrS.ybbR vector containing CBX8 as an insert.

670 Subsequently, EGFP-CBX8 was cloned into the pFBOH-mhl vector cleaved with BseRI via
671 Gibson assembly, with a Serine-Glycine-Serine linker between EGFP and CBX8. Finally, to
672 generate monomeric mEGFP-CBX8, alanine residue 207 in EGFP was mutated to Lysine using
673 a site directed mutagenesis kit (Takeda) and the mutagenesis primers listed in Table 1.

674

675 Table 1: Cloning and mutagenesis primers (5'-3') and sequences

mEGFP mutagenesis A207K fw	CTGAGCACCCAGTCCAAGCTGAG CAAAGACCC	Used for mutagenesis of CBX8- EGFP
mEGFP mutagenesis A207K rv	GGGGTCTTGCTCAGCTTGGACT GGGTGCTCA	Used for mutagenesis of CBX8- EGFP
EGFP_fw_PFBOH_M HL	TTGTATTCAGGGCATGGTGAG CAAGGGCGAG	Used for Gibson assembly of mEGFP-CBX8 into pFBOH-mhl vector
EGFP rv with SGS linker	TGAAAGCTCACTCCACTCTTGTA CAGCTCGTCCATGC	Used for Gibson assembly of mEGFP-CBX8 into pFBOH-mhl vector

CBX8 5' with SGS linker	TGTACAAGAGTGGAAAGTGAGCTT TCAGCGGTGGGG	Used for Gibson assembly of mEGFP-CBX8 into pFBOH-mhl vector
CBX8 rv pFBOH_MHL	CAAGCTTCGTCATCATCATCTTT CTCTTTAAAAAAAGCCT	Used for Gibson assembly of mEGFP-CBX8 into pFBOH-mhl vector
ATOH1 fw	GCAGAGCCAAACATTACACA	Used to amplify ATOH1 from pUC18 plasmid
ATOH1 rv	GCGGAGTTCCCTAAAAGACGCC	Used to amplify ATOH1 from pUC18 plasmid
H2BT120C fw	GTGACCTGCTATAACCAGCAGCAA ATAA	Used for mutagenesis of H2B
H2BT120C rv	GGTATAGCAGGTACGGCTTGG TGCC	Used for mutagenesis of H2B
RING1b pFBOH-mhl fw	ttgtatttccagggcTCTCAGGCTGTG CAGACAAAC	Used for Gibson assembly into pFBOH-mhl vector
RING1b pFBOH-mhl rv	caagcttcgtcatcaTTTGTGCTCCTT GTAGGTGC	Used for Gibson assembly into pFBOH-mhl vector
BMI1 pFBOH-mhl fw	ttgtatttccagggcCATCGAACAAACG AGAATCAAG	Used for Gibson assembly into pFBOH-mhl vector
BMI1 pFBOH-mhl rv	caagcttcgtcatcaACCAGAAGAAG TTGCTGATGA	Used for Gibson assembly into pFBOH-mhl vector
24bp DNA duplex Fluorescein labeled	GGCGCCCTGCCCGCCTCGCTCT G	Fluorescein labeled DNA duplex used for binding assays. Only the top strand is shown. The dye was attached to the 3' end of the top strand.
CBX8 KR21A	ATGGAATTATCAGCAGTAGGTGA ACCGGTGTTGCAGCGGAAGCGC TGCTCAAACGTAGGATTGGAAAG GGTCGCATGGAGTACCTAGTT AAGTGGAAAGGATGGTCACAGA AGTATAGCACATGGGAACCGGA GGAGAACATACTGGATGCTCGCT TGCTAGCAGCGTTGAGGAGCG GGAACGAGAAATGGAGCTGTAC GGACCTAAAAACGTGGACCAA GCCAAAGACCTTCCTTTGAAGG CTCAAGCGGCTGCCAAGGCTGCC ACGTATGAATTAGATCGGATTG TGCCGCAGGTATAAGAATTCCCT	CBX8 KR21A mutant open reading frame (obtained by gene synthesis from GeneScript).

	ACCCAGGGGCCAGTCCACAGGA CTTGGCCTCACGTCTAGGGCA GCAGAGGGCTACGGAACATGG GCCTCTCTCTCCGGCTTCATCTA CTAGTACGAGTAGTACATGTGCC GCGGAAGCGCCAAGGGACGCA GACCGAGACGCAGATCGGGATG CCGAGAGAGATCGGAACGAGA GGCGGAAAGAGAACGCCGAGCGC GAGGCTGAGCGTGAAGCGGAAC GTGGCACAAGCGCCGTTGATGAC AAACCATCGAGCCCTGGTGATT CAGCAAAAACGGGACCCAAG CCTAGGAAGGAGTTGCCGGACCC ATCCAAGCCCCGCTTGGTGAAC CATCGCGGGCCTCGGGGAATAT CTTAAAGGCCGAGCTTGGACGA TACCCCTAGTGGTGCAGGAAAA TTTCTCGGGACATTGGTTATC CAACTTGCTGCACGACAAGACTC AGATTTAGTACAGTGCGGGGTGA CATCCCCCAGCTCTGCAGAG GCGACCGGGGCCCTAGCTGCGA CACCTTCCCAGCACCGTGTAG CGCACCGAGCCGCATTTTAGAA GCTGCTGGCAGGGCGCGCTA GATCCAACGGCACTAGGGTGC GCACGGTTAGGACCTCCCTCGT CCGGGGGGGGCCTATATAGAGA CATGGGAGCTCAGGGGGTAGA CCGTCGCTATCGCTCGTATCCG GTAGCCCCTATTCTGGGTGACCC GGAGGAAGAATCCTGGTCTCCA GTTAACGAATTAGAGAAA GTCGTAGTCACTGACGTTACGTC AAATTTCTGACAGTCACCATCAA AGAGAGCAATACTGATCAAGGGAT TCTTCAAGGAAAAGCGCTAA	
C8_PFB1_68_fw	TTCTGTTCCAGGGGCCGGCCCC AAAAAGCGTGGAA	Primer used to generate the CBX8 ^{ΔChromo} truncation.
C8_PFB1_68_rv	TCGAGACTGCAGGCTTCATCTTT CTCTTAAAAAAGCCT	Primer used to generate the CBX8 ^{ΔChromo} truncation.

676

677

678

679

680 **Protein expression and purification**

681

682 PRC1^{C8}, PRC1 core and CBX8 were co-expressed in *Trichoplusia ni* insect cells using the
683 Baculovirus system. CBX8 variably carried an N-terminal 6xHis-mEGFP or a N-terminal 6xHis-
684 MBP tag. The purification protocols were identical regardless of the tag. Baculoviruses were
685 generated as per manufacturers instructions (Thermo Fisher). The viral titre was determined
686 using the MTT assay (Promega #G3580). *Trichoplusia ni* insect cells were infected at a
687 density of 1.5 - 2 x 10⁶ cells and incubated for 60 hours at 27 °C in a shaker.

688 The cells were spun down at 1500 relative centrifugal force (RCF). The pellet was
689 resuspended in 100 ml of lysis buffer per litre of cell culture (20 mM HEPES-KOH pH 7.5, 400
690 mM NaCl, 25 mM Imidazol, 10 % Glycerol, 0.2 mM TCEP, 1 mM PMSF and EDTA-free
691 Complete protease inhibitor (Thermo Fisher)). Lysis proceeded for 30-45 minutes at 4 °C
692 while rotating. The lysate was then centrifuged at 29000 RCF for 20 minutes at 4 °C. The
693 supernatant was transferred to a fresh tube and 5 ml of Ni-NTA resin (Qiagen) was added.
694 The samples were then incubated for 60 minutes at 4 °C while rotating and subsequently
695 centrifuged at 500 RCF for 5 minutes at 4 °C to settle the beads. About 90 % of the
696 supernatant was removed. The beads were resuspended in the remaining 10 % of
697 supernatant and transferred to 25 mm diameter gravity flow columns (Biorad). The beads
698 were allowed to settle before the remaining buffer was drained and the beads were then
699 washed with 12 CV of Buffer B (20 mM HEPES-KOH pH 7.5 at 20 °C, 500 mM NaCl, 25 mM
700 Imidazole, 10 % Glycerol, 0.2mM TCEP), followed by 30 CV of Buffer A (20 mM HEPES pH 7.5
701 at 20 °C, 100 mM NaCl, 25 mM Imidazole, 10 % Glycerol, 0.5 mM DTT or 0.2 mM TCEP). The
702 protein was then eluted in 6 CV Elution Buffer (20 mM HEPES-KOH pH 7.5 at 20 °C, 100 mM
703 NaCl, 400 mM Imidazole, 10 % Glycerol, 0.2 mM TCEP). The eluted protein was loaded onto
704 a Hitrap 5 ml Heparin column (Cytvia) equilibrated in IX Buffer A (20 mM HEPES pH 7.5 at
705 20 °C, 100 mM NaCl, 0.5 mM DDT or 0.2 mM TCEP) and the column was washed with 5 CV of
706 IX Buffer A. The proteins were resolved over a 20 CV gradient ranging from 0 % to 100 % IX
707 Buffer B (20 mM HEPES pH7.5 at 20 °C, 1000 mM NaCl, 0.5 mM DTT or 0.2 mM TCEP). The
708 fractions were analysed on SDS-PAGE and fractions containing the protein complex of
709 interest with the expected subunits stoichiometry were pooled. The pooled fractions were
710 concentrated using a Amicon ultra 30K centrifugal filter (Merck, cat UFC903024) and
711 purified by size exclusion chromatography using a HiLoad Sephacryl 300 16/60 column
712 (Cytiva) equilibrated in GF Buffer (20 mM HEPES-KOH pH 7.5 at 20 °C, 150 mM NaCl, 0.5 mM
713 DTT). The collected fractions were analysed on SDS-PAGE and fractions containing the
714 protein complex of interest at the expected stoichiometry were pooled and concentrated to
715 a concentration of 1-2 mg/ml using an Amicon ultra 30K centrifugal filter (Merck, cat
716 UFC903024). The purified protein was then aliquoted and frozen in liquid nitrogen. The
717 purified proteins were stored at -80 °C until use.

718

719 For the production of Atto-488 labelled PRC1^{C8} complexes, purification was carried out as
720 above, with some modifications. PRC1^{C8} was purified as described above, without cleaving

721 the N-terminal MBP tag from CBX8, up until the end of the Ion Exchange Chromatography
722 (HiTrap 5 ml Heparin column, as above). Then, fractions containing PRC1^{C8} were pooled
723 together and concentrated to 2.4 mg/ml. To generate untagged PRC1^{C8}, PreScission
724 protease was added to 1:50 protease:PRC1^{C8} mass ratio in a 3.5 ml reaction volume,
725 incubated overnight at 4-8 °C and then the MBP tag was removed using 0.8 ml amylose
726 beads through a batch removal, before proceeding to the subsequent labelling reaction. For
727 the fluorescence labelling of MBP-tagged PRC1^{C8}, the subsequent labelling reaction was
728 carried out without tag cleavage. For fluorescence labelling, of either MBP tagged or
729 untagged PRC1^{C8}, 2.4 mg/ml protein was supplemented with Atto-488 NHS ester (Merck
730 41698; the Atto-488 NHS ester was dissolved in DMSO to 4.3 mM before used) to a final
731 molar stoichiometry of 1.4:1.0 dye:protein and allowed to incubate 1 hour at room
732 temperature in the dark, and then the protein was loaded on a light-protected HiLoad
733 Sephadryl 300 16/60 column equilibrated with 25 mM HEPES-KOH pH 7.5, 0.5 mM DTT, and
734 either 150 mM NaCl or 500 mM NaCl for the MBP-tagged or untagged PRC1^{C8}, respectively.
735 The process was completed as described above, with the exception that the fluorescently
736 labelled proteins were protected from light until experimentation.

737

738 Human UBA1, UBCH5C and Ubiquitin were purified as described previously⁵⁴. Human
739 histone proteins H2A, H2B, H2BT120C, H3 and H4 were purified as described previously⁵⁵,
740 except that the gel filtration step was omitted. Purified *Xenopus laevis* histone proteins H2A,
741 H2B, H3, H4 and H2A acidic patch mutant (E56T, E61T, E64T, D90S, E91T, E92T) were bought
742 from the Histone Source of the Colorado State University, Fort Collins.

743

744

745 **Production and purification of DNA for chromatin reconstitution**

746

747 The ATOH1 polycomb target gene was amplified in a large scale 10 ml PCR reaction including
748 500 nM ATOH1 fwd and reverse primers (see Table 1), 4 µg of ATOH1-pUC18 template⁵¹,
749 200 µM dNTP mix (Invitrogen), 3 % DMSO, 50 mM KCl, 10 mM Tris-HCl, pH 8.8, 1.5 mM
750 MgCl₂, 0.01% sterile gelatin. The reaction mixture was divided into 96-well plates to include
751 50 µl per well and the following PCR program was run:

752

753

Temperature (°C)	Time (minutes)	Number of Cycles
95	3:00	1
95	0:15	
63	0:20	25

72	8:00	
72	3:00	1

754

755

756 The PCR product was purified via ion exchange chromatography using a 5 ml HiTrap Q
757 column (GE Healthcare). The column was equilibrated in Buffer A (25 mM HEPES 7.5, 250
758 mM NaCl) and the sample was resolved using a linear gradient ranging from 0 % to 100 %
759 Buffer B (25 mM HEPES pH 7.5, 2 M NaCl). The fractions containing pure DNA were pooled,
760 subjected to ethanol-precipitation and resuspended in 10 mM Tris-HCl pH 7.5 at 20 °C, 0.1
761 mM EDTA.

762

763 **Chromatin reconstitution**

764

765 Histone Octamers were refolded as described previously⁵⁵. All steps were done at 4 °C or on
766 ice. Chromatin was reconstituted following the salt-gradient dialysis protocol described
767 previously⁵⁵. For large scale reconstitution, DNA and octamer were combined at an optimal
768 ratio that was determined at trial experiments for each batch of octamers and DNA. To
769 determine the optimal ratio of histone octamer to DNA, titration was carried out using
770 increasing amounts of octamer to a constant amount of DNA (molar ratios of 16:1, 18:1,
771 20:1, 22:1 of Octamer:DNA) following by salt gradient dialysis. For the salt gradient dialysis,
772 samples were initially dialysed in a buffer containing 10 mM Tris-HCl pH 7.5 at 20 °C, 2 M
773 KCl, 1 mM EDTA, 1 mM DTT. The initial buffer was then gradually exchanged for a low salt
774 buffer containing 10 mM Tris-HCl pH 7.5 at 20 °C, 250 mM KCl, 1 mM EDTA, 1 mM DTT over
775 the course of 18 hours, after which the salt exchange was complete. Samples were then
776 centrifuged at 21000 RCF for one minute, separated on a 1% agarose gel in TAE buffer and
777 stained with SYBR Safe (Sigma). The highest Octamer:DNA ratio at which chromatin
778 remained soluble after finishing salt dialysis was finally used for large scale reconstitution.
779 For large scale reconstitutions, the salt gradient dialysis was performed as above while
780 scaling up the reaction accordingly. Additionally, after conclusion of the salt gradient, the
781 samples were transferred to 400 ml of low salt buffer (10 mM Tris-HCl pH 7.5 at 20 °C,
782 250 mM KCl, 1 mM EDTA, 1 mM DTT) and dialysed for another 2 hours. The samples were
783 finally dialysed against 1 litre of Chromatin Storage Buffer (10 mM TRIS-HCl pH 7.5, 10 mM
784 KCl) overnight.

785

786 **Reconstitution of Fluorescently labelled chromatin**

787

788 To allow site-specific labelling of histone H2B, a cysteine was introduced via site-directed
789 mutagenesis (H2BK120C, as previously described⁵⁶) using mutagenesis primers indicated in
790 Table S1. H2BK120C was labelled with Cyanine5-maleimide (Lumiprobe cat #13080) as
791 described previously⁵⁶. Labelled octamers were refolded as described above. Before

792 chromatin reconstitution, the unlabelled and labelled octamers were combined at a molar
793 ratio of 7:1 (unlabeled:labelled). Chromatin was then reconstituted as described above.

794

795 **Chromatin condensation assays**

796

797 Fluorescently labelled proteins and chromatin were protected from light whenever possible.
798 Chromatin condensation assays were done as described previously¹⁷ with some
799 modifications. Assays were done in 384-well plates with #1.5 glass bottoms (MatTek
800 PBK384G-1.5-C). The wells were treated with 1 M NaOH for 1 hour at room temperature,
801 NaOH was removed and wells were washed with copious amounts of MilliQ water (MQ).
802 MQ was removed and 70 ul of 5k mPEG-silane (Sigma #JKA3037-1G, dissolved in 95% EtOH
803 to a final concentration of 25 mg/ml) was added to each well. The plates were sealed and
804 incubated overnight at room temperature. The mPEG-silane was removed, the wells were
805 washed once with 95 % EtOH, then rinsed with copious amounts of MQ and dried
806 completely in the fume hood.

807 The wells were then passivated by adding 40 ul of 20 mg/ml BSA (NEB) and incubated for at
808 least one hour at room temperature. The BSA was removed and the wells were washed
809 three times with Condensation Buffer (20 mM HEPES pH 7.5 at 20 °C, 0.2 mg/ml BSA, 10 %
810 Glycerol, 5 mM DTT and 150 mM KCl). The chromatin stock was adjusted to a DNA
811 concentration of 100 ng/ul (unless otherwise stated) and 150 mM KCl. The PRC1 complex
812 was diluted in Condensation buffer to a protein concentration equal to twice the final PRC1
813 assay concentration as stated. To induce condensation, 16 ul of the diluted PRC1 were
814 combined with 16 ul of the salt-adjusted chromatin dilution in PCR tubes. The samples were
815 incubated for 30 minutes at room temperature before being transferred to the 384-well
816 plate and incubated for a further 60 minutes at room temperature, so that the first images
817 were recorded 90 minutes after induction of condensation.

818 Images were recorded with a Nikon C1 scanning confocal microscope. GFP was excited with
819 a 488 nm laser, Cy5 was excited with a 561 nm laser. Linear contrast adjustments were
820 made with ImageJ. Where several micrographs are compared to each other, the same
821 contrast settings were used for all micrographs.

822 For condensation assays in Fig. 2a, Fig. 4, Extended Data Fig. 1d and Extended Data Fig. 9,
823 chromatin and PRC1 dilutions were prepared in Chromatin Buffer (10 mM TRIS-HCl pH 7.5 at
824 20 °C, 10 mM KCl, 1 mM DTT) and PRC1 buffer (20 mM HEPES-KOH pH 7.5 at 20 °C, 150 mM
825 NaCl, 1 mM DTT), respectively. After adjusting BSA and salt concentration and combining
826 PRC1 and chromatin, the final reaction contained the PRC1 and chromatin concentration
827 stated in the figures and the following components: 20 mM HEPES-KOH, pH 7.5, 5 mM TRIS-
828 HCl pH 7.5 at 20 °C, 90 mM KCl, 32.5 mM NaCl, 0.2 mg/ml BSA (NEB), 1mM DTT.

829 DIC images and fluorescence wide field images were recorded with a Leica DMI8 imaging
830 system equipped with a 4.2 MP (2k x 2k) sCMOS monochromatic K8 camera and a 63x oil
831 immersion objective with numerical aperture of 1.3. DIC images in Extended Data Fig. 9
832 were recorded with a Leica DMI8 imaging system equipped with a 4.2 MP (2k x 2k) sCMOS

833 monochromatic DFC 9000GT camera and a 40x dry objective with a numerical aperture of
834 0.8.

835 Condensate quantification was done using ImageJ. A threshold was set for each image to
836 segment condensates in the frame using the Cy5 signal. Condensates overlapping the frame
837 edges were excluded. Then the total area of all condensates in the frame was calculated.

838

839 **Chromatin ubiquitylation assay**

840

841 The salt concentration of the chromatin stock was adjusted to 100 mM KCl. The nucleosome
842 equivalent concentration of chromatin arrays was calculated by measuring the molar DNA
843 concentration and assuming that one DNA molecule is populated by 20 nucleosomes. The
844 reaction mixture included 750 nM (Fig. 1d) or 1000 nM (Extended Data Fig.1d) of chromatin
845 (nucleosome equivalent concentration), 500 nM PRC1^{C8} or RING1b-BMI1 dimer, 100 nM
846 hUBA1, 500 nM UBCH5C and 50 µM ubiquitin in Ub-Buffer (25 mM HEPES-KOH pH 7.5 at
847 20 °C, 100 mM KCl, 3 mM MgCl and 2 mM DTT) and started by adding ATP to a final
848 concentration of 3 mM. 15 µl reactions were incubated at 30 °C for 45 minutes or the
849 indicated time points (Extended Data Fig 1d). The reaction was stopped by adding 5 µl of 4X
850 NuPage LDS-loading dye (Thermo Scientific cat #NP0008) supplemented with 5 % 2-
851 mercaptoethanol. The samples were separated on a 4-12% NuPage gel (Thermo Scientific
852 cat #NP0321BOX) using MES buffer (Thermo Scientific cat #NP0002) in the tank. The gels
853 were then blotted onto a nitrocellulose membrane (Amersham, cat #GE10600002) in Tris-
854 Glycine transfer buffer + 20 % Ethanol (v/v) for 90 minutes in the cold room at 310 mAmp in
855 a blotting tank (BioRad). H2A was detected using anti-H2A primary antibodies (Merck
856 Millipore Cat. # 07-146, 1:1000 titer) and HRP-conjugated secondary antibodies (Santa Cruz,
857 cat #sc-2357, titer 1:5000).

858

859 **Sample preparation for cryo-electron tomography**

860

861 The PRC1^{C8} complex (MBP-tagged CBX8) was combined with chromatinized ATOH1 at a final
862 concentration of 1.6 µM PRC1^{C8} and 500 ng/µl DNA at a final salt concentration of 25 mM
863 NaCl and 8.3 mM KCl. Samples were incubated at room temperature for 30 minutes. Just
864 before freezing, 5 nm gold nanoparticles were added at a 1:6 ratio (v/v). 3.5 µl of sample
865 was applied to a Quantifoil grid (R1.2/1.3 on 200 copper mesh, Quantifoil cat #N1-
866 C14nCu20-01) and vitrified in liquid ethane using the Vitrobot plunge freezer (Thermo
867 Scientific) with the following settings: Temperature 4°C, blot force -3, blot time 4 seconds,
868 humidity 100%. The final sample composition after addition of gold was 1330 nM PRC1^{C8}
869 and 3500 nM chromatin (estimated nucleosome concentration) in 3.5 mM HEPES-KOH pH
870 7.5, 6.8 mM TRIS-HCl PH 7.5, 21 mM NaCl, 7 mM KCl, 0.8 mM DTT. The sample of chromatin
871 in absence of PRC1 was prepared the same but instead of adding PRC1 an equivalent
872 volume of the PRC1 buffer was added.

873

874 **Low magnification cryo-EM image collection**

875

876 The images in Extended Data Fig. 3a were collected just before cryo-ET data collection using
877 the Titan Krios (Thermo Fisher) at an acceleration voltage of 300 keV and are of the same
878 grid from which tomograms were collected. The images in Extended Data Fig. 4a were
879 recorded using a Talos Arctica TEM (Thermo Fisher) at an acceleration Voltage of 200 keV.

880

881 **Cryo-electron tomography data collection and processing**

882

883 The data was collected with a Titan Krios electron microscope (Thermo Fisher) at 300 keV
884 acceleration voltage using a Gatan K2 (+PRC1 sample) or K3 (-PRC1 sample) Summit camera
885 (Gatan). A tilt series was acquired ranging from -60 to 60 degrees with 3 degree increments
886 and a nominal defocus of -2.5 μ m. A dose symmetric collection scheme was followed as
887 described previously⁵⁷. Chromatin in the presence of PRC1 was images at pixel size of 1.32
888 Angstrom. The chromatin samples in the absence of PRC1 were collected in super resolution
889 mode with a nominal pixel size of 1.632 Angstrom (0.815 Angstrom super resolution pixel
890 size). The total dose per tomogram was 144.32 e/A² (+PRC1) and 160.72 e/A² (-PRC1). Four
891 frames were collected per tilt (dose per frame 0.88 e/A² for the +PRC1 sample and 0.98 e/A²
892 for the -PRC1 sample). The movies were motion corrected using motioncor2⁵⁸. The motion
893 corrected images were combined into stacks and further processed with Imod⁵⁹ version
894 4.9.9. Imaging artefacts were identified and removed with Imod's Ccderaser function. Tilts
895 were aligned using the gold fiducial markers and the final aligned stack was binned by a
896 factor of 4. The defocus was estimated using emClarity⁶⁰ and the estimated defocus was
897 used in Imod for CTF correction. The final tomogram was calculated using Imod's
898 implementation of weighted back projection. For visualisation, the tomogram was denoised
899 using Topaz⁵⁰. The denoised tomogram was only used for visualisation (Figure 1 and Movie
900 S1). The original non-denoised tomograms were used for all further processing, including
901 template matching and subtomogram averaging.

902

903 **Template matching, subtomogram averaging and modelling the chromatin structure of
904 condensates from cryo-electron tomograms**

905 Two tomograms were selected for further processing (Tomogram #1 and Tomogram #2 in
906 the following). To avoid user bias, we used a template matching algorithm⁶¹ with the
907 structure of a single nucleosome as template (EMD-8140⁶¹) to identify initial positions and
908 orientations for each nucleosome. The pixel size of the template was adjusted using
909 emClarity (version 1.0.0) to match the unbinned pixel size of the tomogram⁶⁰. The template
910 was then subjected to a low-pass filter of 30 Angstrom and binned by a factor of four to
911 match the binned tomogram. Template matching was done with the Matlab
912 implementation of Dynamo (version v-1.1.514)⁶¹ using the "dynamo_match" function. The
913 template was masked with a tight-fitting mask with smooth edges. The scanning range was

914 set to 360 degrees with 10 degree steps. In-plane rotation was also scanned over 360
915 degrees with 10 degrees steps. Particles that passed a cross-correlation cut-off of 0.17
916 (Tomogram #1), 0.19 (Tomogram #2), 0.24 (Tomogram #27), 0.23 (Tomogram #41) and 0.25
917 (Tomogram #49) were selected for further analysis. Obvious false positives were removed
918 manually.

919 The particles were cropped from the tomogram with a box size of 36 pixels. Nucleosome
920 position and orientation was refined over three rounds of subtomogram averaging⁶¹. As an
921 initial template for subtomogram averaging, we used an average from all cropped particles
922 after template matching, masked with a tight-fitting mask with smooth edges generated in
923 the Dynamo mask editor. Specific settings for the different rounds of subtomogram
924 averaging are detailed in Table 2. The resulting average structure of a nucleosome from the
925 subtomogram averaging was then used to populate a volume the size of the tomogram with
926 nucleosomes at the determined positions and orientations. The graphic depiction of the
927 final model (Figure 1G) was generated using the Dynamo Matlab implementation⁶¹.
928

929 Table 2: Settings for subtomogram averaging in Dynamo

	Round 1	Round 2	Round 3
Iterations	3	3	3
References	1	1	1
Cone Aperture	100	16	8
Cone Sampling	5	2	1
Azymuth Rotation Range	100	16	8
Azymuth Rotation Sampling	5	2	1
Refine	0	0	4
Refine Factor	0	0	2
High Pass	2	2	2
Low Pass	7	8	8

Symmetry	c1	c1	c1
Particle Dimension	36	36	36
Shift Limits	5	4	2
Shift Limiting Ways	1	1	1
Separation in Tomogram	0	0	0
Basic MRA	0	0	0
Threshold Parameter	0.5	0.6	0.6
Threshold Modus	2	2	2

930

931

932 **Analysis of exclusion volume**

933

934 Exclusion volumes for spherical molecules of various radii were calculated using 3V²⁶ as
935 follows. First, the positional and rotational coordinates of the nucleosomes within
936 Tomogram #1 were determined by template matching followed by subtomogram averaging,
937 as described above. Next, the positional and rotational coordinates of the nucleosomes
938 were tabulated from within a section of 300 pixels x 300 pixels x 150 pixels (corresponding
939 to 158.4 nm x 158.4 nm x 87.0 nm at the x, y and z axes, respectively) centred on the pixel at
940 location (650,650,80), which was large enough to include hundreds of nucleosomes but yet
941 sufficiently small to carry out the subsequent computational analysis. The dimensions of the
942 resulting table were converted to Angstrom by multiplying with a tomogram pixel size of
943 5.28 Angstrom/pixel. Next, the table including nucleosome positions was used by the
944 Dynamo function 'dtchimera' to generate a chimera cmd script that placed a pdb structure
945 of a single nucleosome (PDB 1KX4⁶³) at the position and orientation defined for each
946 nucleosome in the table. At the end of this process, each of the nucleosomes within the
947 tomogram section is represented by the pdb coordinates of the nucleosome template. The
948 resulting model was saved as a pdb file and used as input for 3V²⁶. Varying probe radii
949 ranging from 2 to 20 nm were used.

950

951

952

953

954 **Hydrodynamic radius calculation using protein structures**

955

956 The hydrodynamic radii of various proteins (Figure 1I) were calculated using the HullRad³⁹
957 web server (<http://52.14.70.9/>). The PDB codes for the structures used are: 6LTJ (BAF⁴⁵),
958 1MUH (Tn5⁴⁰), 7O4J (PolII-PIC⁴⁷), 6C24 (PRC2.2⁶⁴), 8GXS (PolII-Mediator⁶⁵). 6LTJ, 6C24, 8GXS
959 and 7O4J are only partial models as not all residues were assigned, therefore the calculated
960 hydrodynamic radius represents an estimate of the minimal complex size, while the actual
961 size of these complexes could be larger.

962

963 **Analysis of nucleosome-nucleosome orientation and distances**

964

965 Nucleosome-nucleosome orientation was classified into face-face, face-side and side-side,
966 as described in²². The orientations were calculated from the output table of the template
967 matching and subtomogram averaging process in Dynamo⁶¹ using the Matlab script
968 'calculate_orientation.m'. The nucleosome-nucleosome orientation plot (Fig. S1A) was
969 generated using the 'plot_edges' function from the python notebook
970 NCP_orientation_analysis.ipyn. Both scripts are available on Github
971 (<https://github.com/MichaUckelmann/Chromatin-Structure-Analysis>).
972 Centre-centre distances between neighbouring nucleosomes were calculated using the
973 Matlab function 'knnsearch'. Double-counted distances were removed before further
974 analysis.

975

976 **Cryo-light microscopy**

977

978 The samples were prepared as described for cryo-electron tomography, without gold
979 nanoparticles and in a buffer containing 100 mM KCl. The vitrified grids were imaged using a
980 ZEISS LSM900 Airyscan2 with a Linkam CMS196V Cryo stage.

981

982 **Fluorescence recovery after photobleaching (FRAP)**

983

984 For FRAP of PRC1^{C8} that was fluorescently labelled using a GFP-CBX8, samples and plates
985 were prepared and images were recorded as described above for chromatin condensation
986 assays. 1 μM PRC1^{C8} with an N-terminal GFP tag was used. The FRAP experiments were set
987 up with the NIS-Elements software (Nikon). Regions of interest (ROIs) were defined and a
988 single image was recorded before bleaching. Then the ROI was bleached using 488 nm (GFP)
989 and 561 (Cy5) lasers. The bleaching time and laser power was set so that approximately
990 80 % of fluorescence signal within the ROI was quenched. Recovery was measured over 424
991 seconds, recording a total of 13 images. The data was analysed with ImageJ, the mean pixel
992 intensity of the bleached ROI was quantified for each timepoint.

993 For FRAP of PRC1^{C8} that was fluorescently labelled using spared labelling of lysine
994 residues using Atto-488, samples and plates were prepared and images were recorded as

995 described above for chromatin condensation assays. To bring both the untagged PRC1^{C8} and
996 the MBP-tagged PRC1^{C8} (i.e. an N-terminal MBP tag on CBX8) to the same concentration, the
997 stock solutions of the Atto-488-labelled untagged PRC1^{C8} was adjusted to 8 μ M PRC1^{C8}, 150
998 mM NaCl and 25mM HEPES pH7.5. Both the PRC1^{C8} stocks, with or without the MBP tag,
999 were then diluted to 4 μ M protein in a condensation buffer (25 mM HEPES pH7.5, 150 mM
1000 KCl, 0.2 mg/mL BSA, 2 mM DTT). 8 μ l of 4 μ M PRC1 solution and 8 μ l of 100 ng/ μ l chromatin
1001 (DNA concentration) were combined in a well to induce condensation, at final
1002 concentrations of 2 μ M PRC1^{C8}, with or without the MBP tag, 50 ng/ μ l chromatin (DNA
1003 concentration) and with a final buffer composition of 25 mM HEPES pH7.5, 37.5 mM NaCl,
1004 112.5 mM KCl, 0.1 mg/mL BSA and 1 mM DTT. Regions of interest (ROI) were defined and a
1005 single image was recorded before bleaching. Then the ROI was bleached using 488 nm
1006 (Atto-488) and 561 nm (Cy5) lasers. The bleaching time and laser power were set so that
1007 approximately 80 % of the fluorescence signal within the ROI was quenched. Recovery was
1008 measured over 24 minutes, with a frequency of \sim 1 image/minute. The data was analysed
1009 with NIS-Elements software.

1010

1011 **Single molecule confocal microscopy**

1012

1013 Cy5 labelled reconstituted chromatin (200 nM nucleosome concentration) and GFP labelled
1014 PRC1^{C8} at the concentration indicated in the figure were combined in assay buffer (25 mM
1015 HEPES-KOH pH 7.5, 100 mM KCl, 15 mM NaCl, 1 mM DTT, 0.1 mg/ml BSA). Samples were
1016 immediately loaded into a custom-made silicone well plate with a 70 x 80 mm glass
1017 coverslip (ProSciTech, Kirwan, QLD, Australia). Plates were analysed at room temperature on
1018 a custom setup based on a Zeiss Axio Observer microscope (Zeiss, Oberkochen, Germany).
1019 Illumination is provided by a 488 nm and a 561 nm laser beams, cofocussed in the sample
1020 volume using a \times 40 magnification, 1.2 Numerical Aperture water immersion objective (Zeiss,
1021 Oberkochen, Germany). This creates a very small observation volume in solution (\sim 1 fL),
1022 through which fluorescent proteins diffuse and emitting light in specific wavelengths as their
1023 fluorescent tags are excited by the laser beams. Light emitted by the fluorophores is split
1024 into GFP and mCherry channels by a 560 nm dichroic mirror. The fluorescence of GFP is
1025 measured through a 525/50 nm band-pass filter and the fluorescence of mCherry is
1026 measured through a 580 nm long-pass filter. Fluorescence is detected by two photon
1027 counting detectors (Micro Photon Devices, Bolzano, Italy). Photons of the two channels are
1028 recorded simultaneously in 1 ms time bins by a custom Lab-VIEW 2018 program (National
1029 Instruments)⁶⁶. The data were analysed using a custom python script (Spyder version 4.1.5)
1030 that automatically detects peaks, as described in^{67,68}.

1031

1032 **DNA binding assays**

1033

1034 DNA binding was assayed using a 24 bp DNA (sequence see Table 1) with Fluorescein
1035 attached to the top strand. The probe was protected from light wherever possible. The

1036 probes were synthesised and delivered as duplexes (IDT). Probes were dissolved at a
1037 concentration of 5 mM DNA in milliQ water. The probes were then diluted to 4 μ M in
1038 annealing buffer (20 mM HEPES-KOH, 150 mM NaCl) and heated to 95 °C for 5 minutes. The
1039 probe was then left at room temperature for at least 1 hour to anneal before being diluted
1040 to 20 nM in 20 mM HEPES-KOH pH 7.5 at 20 °C, 150 mM NaCl, 1 mg/ml BSA (NEB cat
1041 #B9000S), 0.1% Tween20, 1 mM DTT. Serial protein dilutions of the PRC1^{C8} and RING1b-
1042 BMI1 complexes were prepared in Protein Dilution Buffer (20 mM HEPES-KOH, 150 mM
1043 NaCl, 1 mM DTT) ranging from 8000 nM to 3.9 nM (Fig. 3) and from 7200 nM to 7 nM (Fig.
1044 4). 20 μ l of probe were mixed with 20 μ l of the respective protein dilution and transferred to
1045 a 384-well plate. The samples were incubated for 30 minutes in the dark at room
1046 temperature and then read using a Pherastar plate reader (BMG Labtech). The fluorescence
1047 anisotropy signal was normalised and the curves were fitted with a specific binding model
1048 with Hill slope (GraphPad Prism).

1049

1050 **Crosslinking mass spectrometry (XL-MS)**

1051

1052 Sample preparation, processing and data analysis was identical for samples with and
1053 without chromatin. Reconstituted chromatin (if used) was dialysed overnight against 1 litre
1054 of XL buffer (25 mM HEPES-KOH pH 7.5 at 20 °C, 150 mM NaCl, 1 mM DTT). The chromatin
1055 was combined with PRC1^{C8} in a 1:1.5 molar ratio (Nucleosomes:PRC1^{C8}). Specifically, the
1056 nucleosome equivalent concentration of the chromatin array was calculated from the
1057 measured DNA concentration assuming 18 nucleosomes per DNA molecule. 1.5 μ M PRC1
1058 and 1 μ M nucleosome equivalent concentration of chromatin arrays were then combined in
1059 XL buffer and incubated for 30 minutes at room temperature. Crosslinking was done as
1060 described before⁶⁹. The bis(sulfosuccinimidyl)suberate (BS3) crosslinker was added to a final
1061 concentration of 500 μ M and crosslinking proceeded for 20 minutes at room temperature at
1062 a reaction volume of 15 μ l. The reaction was stopped by the addition of Tris-HCl pH 8 at
1063 20 °C to a final concentration of 125 mM. The samples were then diluted to a volume of
1064 100 μ L using a buffer containing 50 mM Tris pH 8 at 20 °C and 150 mM NaCl. TCEP was
1065 added to a final concentration of 10 mM and the samples were incubated at 60 °C for
1066 30 min. Chloroacetamide was added to a final concentration of 40 mM and the samples
1067 were incubated in the dark for 20 min. The samples were then digested using trypsin
1068 (Promega cat #V5280) at 37 °C overnight. The digest was stopped by adding formic acid to a
1069 final concentration of 1% v/v. The digested samples were purified using 100 μ l ZipTip pipette
1070 tips (Merck cat #ZTC18S960) according to the manufacturer's instructions. Samples were
1071 then concentrated to ~5 μ L using a SpeedVac vacuum centrifuge and diluted with 20 μ L
1072 Buffer A (0.1% v/v formic acid).

1073

1074 The peptides were analyzed by online nano-high-pressure liquid chromatography (UHPLC)
1075 electrospray ionization-tandem mass spectrometry (MS/MS) on an Q Exactive Plus
1076 Instrument connected to an Ultimate 3000 UHPLC (Thermo-Fisher Scientific). Peptides

1077 reconstituted in 0.1% formic acid were loaded onto a trap column (Acclaim C18 PepMap 100
1078 nano Trap, 2 cm × 100 µm I.D., 5-µm particle size and 300-Å pore size; Thermo-Fisher
1079 Scientific) at 15 µL/min for 3 min before switching the precolumn in line with the analytical
1080 column (Acclaim C18 PepMap RSLC nanocolumn, 75 µm ID × 50 cm, 3-µm particle size, 100-
1081 Å pore size; Thermo-Fisher Scientific). The separation of peptides was performed at
1082 250 nL/min using a non-linear acetonitrile (ACN) gradient of buffer A (0.1% formic acid) and
1083 buffer B (0.1% formic acid, 80% ACN), starting at 2.5% buffer B to 42.5% over 95 min. Data
1084 were collected in positive mode using a Data Dependent Acquisition m/z of 375–2000 as the
1085 scan range, and higher-energy collisional dissociation (HCD) for MS/MS of the 12 most
1086 intense ions with z 2–5. Other instrument parameters were: MS1 scan at 70,000 resolution,
1087 MS maximum injection time 118 ms, AGC target 3E6, ion intensity threshold of 4.2e4 and
1088 dynamic exclusion set to 15 s. MS/MS resolution of 35000 at Orbitrap with the maximum
1089 injection time of 118 ms, AGC of 5e5 and HCD with collision energy = 27%.
1090 For the data analysis, Thermo raw files were analysed using the pLink 2.3.4 search engine⁷⁰
1091 to identify crosslinked peptides, searching against the sequences of RING1b, BMI1, CBX8,
1092 H2A, H2B, H3 and H4. The default settings for searches were used. N-terminal acetylation
1093 and methionine oxidation were used as variable modifications and carbamidomethyl on
1094 cysteines as a fixed modification. False discovery rates of 1% for peptide spectrum match
1095 level were applied by searching a reverse database. Crosslinked peptides were further
1096 analysed using the crisscrosslinkeR package⁷¹. Specifically, peptides were retained by
1097 crisscrosslinkeR only if they passed a p-value cutoff of 0.05 or were present in at least two of
1098 three replicates. Subsequent visualisation of retained peptide was carried out with xiNET⁷².
1099

1100 **Generation of Cbx8 KO mESC lines using CRISPR/Cas9**

1101
1102 Paired sgRNAs were designed to delete exons 1–4 of the murine *Cbx8* gene. The Golden
1103 Gate Cloning method was used to clone the sgRNAs (sequence below) into the lentiguide-
1104 mCherry-Cas9 plasmid^{73,74}. 2 million mESCs were transfected with 1 µg of each plasmid
1105 carrying sgRNAs-mCherry-Cas9, using electroporation (Neon™ Transfection System
1106 MPK5000). The following day, mCherry-positive mESCs were sorted by FACS and plated on a
1107 10 cm dish at a very low density for single-cell clone picking. After 5–6 days, individual
1108 colonies (derived from single cells) were picked, expanded, and genotyped using genomic
1109 PCR to identify homozygous/biallelic deletions of Cbx8 KO mESC colonies. Selected Cbx8 KO
1110 mESC lines were further confirmed by western blot for CBX8 (Cell Signalling, CBX8 (D2O8C),
1111 cat # 14696S, titer 1:50 (Fig. 4a)) and HRP-conjugated secondary antibodies (Santa Cruz, cat
1112 #sc-2357, titer 1:10000).

1113

1114 **Cbx8 sgRNA sequences (5' and 3' sgRNAs)**

1115 CBX8-5'Fw: CACCTGCGAATGCGCCGCTTCAGG

1116 CBX8-5'Rv: AAACCCTGAAGCGGGCGCATTGCA

1117 CBX8-3'Fw: CACCCTCTATGGCCCCAAAAAGCG

1118 CBX8-3'Rv: AAACCGCTTTGGGCCATAGAG

1119

1120 **Cbx8 genotyping primers:**

1121 Deletion_Fw: GCCTTCTGGTGCAGCTAAGT

1122 Deletion_Rv: GACGTCAGCAGGAGAGTATT

1123 Internal_Fw: CACCAAATGAATGCTCCAAA

1124 Internal_Rv (same as the Deletion_Rv): GACGTCAGCAGGAGAGTATT

1125

1126 **Mouse embryonic stem cell culture**

1127

1128 Wildtype and *Cbx8* knockout mES cells were grown on gelatinized culture dishes in DMEM,
1129 20 % FBS, 1x non-essential amino acids (Gibco #11140-050), 1x Glutamax (Gibco #35050-
1130 061), PenStrep 100 u/ml (Thermo Fischer), 0.5 x EmbryoMax 2-Mercaptoethanol (Merck
1131 Millipore #ES-007-E), 2.5 µg/ml Plasmocin (Invivogen), 1000 U/ml ESGRO Leukemia
1132 Inhibitory Factor (LIF) (Merck Millipore cat #ESG1107). For ATAC-seq experiments with the
1133 reporter-integrated mECS line, the cells were treated for 6 days with 1 µg/ml Doxycycline
1134 (passaged every 48 h) before ATAC-seq was performed as described below.

1135

1136 **Mouse embryonic stem cell differentiation ahead of ChIP-seq and ATAC-seq**

1137

1138 Differentiation was induced by seeding cells at a density of 0.3×10^6 cells per well in 6-well
1139 plates (for ATAC-seq) or at 1.5×10^6 cells per 10-cm culture dish (for ChIP-seq) in media
1140 containing 1 µM all-trans retinoic acid (RA, Sigma-Aldrich R2625-50MG) and no LIF. Cells
1141 were differentiated for 48 hours and the media was changed after 24 hours. Control cells
1142 were treated with a DMSO volume equivalent to the RA volume in the differentiating cells.
1143 After 48 hours, the cells were harvested, washed once with PBS, counted and used
1144 immediately in either ChIP-seq or ATAC-seq experiments.

1145

1146 **Mouse embryonic stem cell culture for ChIP-qPCR**

1147

1148 TetR-CBX8 reporter-integrated mESCs were cultivated without feeders in high-glucose-
1149 DMEM (Corning 10-013-CV) supplemented with 13.5% fetal bovine serum (Corning 35-015-
1150 CV), 10 mM HEPES pH 7.4 (Corning, 25-060-CI), 2 mM GlutaMAX (Gibco, 35050-061), 1 mM
1151 Sodium Pyruvate (Corning 25-000-CI), 1% Penicillin/Streptomycin (Sigma, P0781), 1X non-
1152 essential amino acids (Gibco, 11140-050), 50 mM β-mercaptoethanol (Gibco, 21985-023)
1153 and recombinant LIF. Cells were incubated at 37 °C and 5 % CO₂ and were passaged every
1154 48 h by trypsinization in 0.25 % 1x Trypsin-EDTA (Gibco, 25200-056). To reverse TetR-CBX8
1155 binding, 1 µg/ml Doxycycline (Sigma, D9891) was added to cell culture medium for 6 hours.

1156

1157

1158

1159 **ChIP qPCR**

1160

1161 25 x 10⁶ reporter-integrated mESCs were collected, washed once in 1x PBS and cross-linked
1162 for 7 min in 1 % formaldehyde. The crosslinking was quenched by addition of 125 mM
1163 glycine and incubated on ice. The cross-linked ESCs were pelleted by centrifugation for 5 min
1164 at 1200 g at 4 °C. Nuclei were prepared by washes with NP-Rinse buffer 1 (10 mM Tris pH
1165 8.0, 10 mM EDTA pH 8.0, 0.5 mM EGTA, 0.25 % Triton X-100) followed by NP-Rinse buffer 2
1166 (10 mM Tris pH 8.0, 1 mM EDTA, 0.5 mM EGTA, 200 mM NaCl). Afterwards, the nuclei were
1167 washed twice with shearing buffer (1 mM EDTA pH 8.0, 10 mM Tris-HCl pH 8.0, 0.1 % SDS)
1168 and subsequently resuspended in 900 µL shearing buffer including 1x protease inhibitors
1169 Complete Mini cocktail (Roche). Chromatin was sheared by sonication in 15 ml Bioruptor
1170 tubes (Diagenode, C01020031) with 437.5 mg sonication beads (Diagenode, C03070001) for
1171 6 cycles (1 min on and 1 min off) on a Bioruptor Pico sonicator (Diagenode). ChIP lysates
1172 equivalent to 50 ug DNA were incubated in 1x IP buffer (50 mM HEPES/KOH pH 7.5, 300 mM
1173 NaCl, 1 mM EDTA, 1% Triton X-100, 0.1% DOC, 0.1% SDS), and 1.5 ul of FLAG M2 antibody
1174 (Sigma Aldrich Sigma F1804) overnight. Antibody-bound chromatin was captured using
1175 Dynabeads protein G beads (Thermofisher #10004D) for 4 h at 4 °C. ChIPs were washed 5x
1176 with 1x IP buffer (50 mM HEPES/KOH pH 7.5, 300 mM NaCl, 1 mM EDTA, 1% Triton-X100,
1177 0.1 % DOC, 0.1 % SDS), followed by 3x washes with DOC buffer (10 mM Tris pH 8, 0.25 mM
1178 LiCl, 1 mM EDTA, 0.5 % NP40, 0.5 % DOC) and 1x with TE/50 mM NaCl. ChIP DNA was eluted
1179 twice with elution buffer (1 % SDS, 0.1 M NaHCO₃) at 65 °C for 20 min, and subsequently
1180 treated with RNase A (60 ug final, Invitrogen) for 30 min at 37 °C, and Proteinase K (15ug,
1181 NEB) for 3 h at 55 °C and crosslinks were reversed overnight at 65 °C. The following day, ChIP
1182 samples and corresponding inputs were purified by AMPure XP beads (Beckman Coulter
1183 A63880).

1184

1185 ChIP-qPCR primers:

Name	Forward primer sequence	Reverse primer sequence
TetO	AAGATGGCTGCAGGAATT	ATACACGCCCTACCTCGACATAC
+0.6 kb	GCAGGACGTGACAAATGGAAG	AAAGCGAAGGAGCAAAGCTG
+1.0 kb	GATCCGGACCGCCACATC	ACACCTTGCCGATGTCGAG
+1.9 kb	CAGTGCCACGTTGTGAGTTG	GCCCCCTGTTGAATACGCTTG
IAP	CTCCATGTGCTCTGCCTTCC	CCCCGTCCCTTTAGGAGA

1186

1187 **ChIP-seq**

1188

1189 ChIP-seq was done as described previously⁷⁵. 1.5 µg of CBX8 antibody (Cell Signalling, CBX8
1190 (D2O8C), cat # 14696S) and 3 µg of H3K27me3 antibody (Tri-Methyl-Histone H3 (Lys27)
1191 (C36B11), cat #35861SF) were used. Libraries were prepared using NEBNext ultra II DNA
1192 library kit for Illumina (NEB Biolabs) according to the manufacturer instructions. The

1193 resulting libraries were assessed for quality on a High Sensitivity D1000 Screen Tape
1194 (Agilent) and were sequenced using an Illumina Novaseq 6000 sequencer (Genewiz/Azenta).
1195

1196 **Data processing for Chip-seq**

1197

1198 The reads were quality-trimmed and adapters were removed using Trim Galore!, a wrapper
1199 script to cutadapt⁷⁶, in paired end mode and using default settings. The reads were then
1200 aligned to the mouse mm10 genome build using bowtie2 (version 2.3.5)⁷⁷ with the option
1201 “very-sensitive”. The data was reduced to only properly paired reads using “samtools view”
1202 (Samtools version 1.9) with the flag “-f 3”. PCR duplicates were removed using the
1203 RemoveDuplicates function from Picard Tools (version 2.19.0). Read mates were fixed using
1204 samtools fixmate. BigWig files were calculated using BamCoverage (Deeptools version 3.5.2)
1205 with CPM normalisation.

1206 Peaks were called with Macs2 (version 2.1.1)⁷⁸ callpeak function, using the input sample as
1207 control. For the CBX8 ChIP-seq data set, default settings with a q-value cut-off of 0.05 were
1208 used. For H3K27me3 ChIP-seq data set, broad mode was used with a q-value and broad
1209 cutoff of 0.001. Peaks overlapping with ENCODE blacklisted regions⁷⁹ were removed.
1210

1211 **ATAC-seq**

1212

1213 ATAC-seq was done using a commercial kit (Diagenode Cat.# C01080002) according to the
1214 instructions of the manufacturer. The resulting libraries were assessed for quality control on
1215 a High Sensitivity D1000 Screen Tape (Agilent) and libraries were sequenced using an
1216 Illumina Novaseq 6000 sequencer (Genewiz/Azenta).
1217

1218 **Data processing ATAC-seq**

1219

1220 ATAC-seq data was processed as described previously⁸⁰. Specifically, reads were quality-
1221 trimmed and adapters were removed using Trim Galore!, a wrapper script to cutadapt⁷⁶, in
1222 paired end mode using default settings. The reads were then aligned to the mouse mm10
1223 genome build using bowtie2 (version 2.3.5)⁷⁷ with the option “very-sensitive”. Reads were
1224 sorted and indexed using Samtools (version 1.9). Mitochondrial reads were removed using a
1225 python script from Harvard Bioinformatics (available at
<https://github.com/harvardinformatics/ATAC-seq>). The data was reduced to only properly
1226 paired reads using “samtools view” with the flag “-f 3”. The library complexity was
1227 estimated and the data sets were subsampled to reach a similar complexity as described
1228 previously⁸⁰. Data shown in Fig. 5h and Extended Data Fig 8b were not subsampled because
1229 complexity was nearly identical. PCR duplicates were removed using the RemoveDuplicates
1230 function from Picard Tools (version 2.19.0). Read mates were fixed using samtools fixmate.
1231 BigWig files were calculated using BamCoverage (Deeptools version 3.5.2) with CPM
1232 normalisation
1233

1234 For peak calling the bam files were converted to BEDPE files and the Tn5 shift was corrected
1235 by running a bash script provided at <https://github.com/reskejak/ATAC-seq>
1236 (bedpeTn5Shift.sh). Files were then converted to minimal bed format and peaks were called
1237 using Macs2 (version 2.1.1)⁷⁸ callpeak function in broad mode with broad-cutoff set to 0.05.
1238 Peaks overlapping with ENCODE blacklisted regions⁷⁹ were removed. Consensus peaks for
1239 each condition were defined as the intersect of peaks from both biological replicates. Venn
1240 diagrams were generated using the ChIPPeakAnno package⁸¹.

1241

1242

1243

1244

1245

1246

1247 **References**

- 1248 1. Misteli, T. The Self-Organizing Genome: Principles of Genome Architecture and
1249 Function. *Cell* **183**, 28–45 (2020).
- 1250 2. Schuettengruber, B., Bourbon, H.-M., Di Croce, L. & Cavalli, G. Genome Regulation by
1251 Polycomb and Trithorax: 70 Years and Counting. *Cell* **171**, 34–57 (2017).
- 1252 3. Blackledge, N. P., Rose, N. R. & Klose, R. J. Targeting Polycomb systems to regulate
1253 gene expression: modifications to a complex story. *Nat Rev Mol Cell Biol* **16**, 643–649
1254 (2015).
- 1255 4. Eskeland, R. *et al.* Ring1B Compacts Chromatin Structure and Represses Gene
1256 Expression Independent of Histone Ubiquitination. *Molecular Cell* **38**, 452–464 (2010).
- 1257 5. Francis, N. J., Kingston, R. E. & Woodcock, C. L. Chromatin Compaction by a Polycomb
1258 Group Protein Complex. *Science* **306**, 1574–1577 (2004).
- 1259 6. Grau, D. J. *et al.* Compaction of chromatin by diverse Polycomb group proteins requires
1260 localized regions of high charge. *Genes Dev.* **25**, 2210–2221 (2011).
- 1261 7. Lau, M. S. *et al.* Mutation of a nucleosome compaction region disrupts Polycomb-
1262 mediated axial patterning. *Science* **355**, 1081–1084 (2017).
- 1263 8. Isono, K. *et al.* SAM Domain Polymerization Links Subnuclear Clustering of PRC1 to
1264 Gene Silencing. *Developmental Cell* **26**, 565–577 (2013).
- 1265 9. Tatavosian, R. *et al.* Nuclear condensates of the Polycomb protein chromobox 2 (CBX2)
1266 assemble through phase separation. *Journal of Biological Chemistry* **294**, 1451–1463
1267 (2019).
- 1268 10. Plys, A. J. *et al.* Phase separation of Polycomb-repressive complex 1 is governed by a
1269 charged disordered region of CBX2. *Genes Dev.* **33**, 799–813 (2019).
- 1270 11. Illingworth, R. S. Chromatin folding and nuclear architecture: PRC1 function in 3D.
1271 *Current Opinion in Genetics & Development* **55**, 82–90 (2019).
- 1272 12. Miron, E. *et al.* Chromatin arranges in chains of mesoscale domains with nanoscale
1273 functional topography independent of cohesin. *Science Advances* **6**, eaba8811 (2020).

1274 13. Nozaki, T. *et al.* Dynamic Organization of Chromatin Domains Revealed by Super-
1275 Resolution Live-Cell Imaging. *Molecular Cell* **67**, 282-293.e7 (2017).

1276 14. Murphy, S. & Boettiger, A. N. Polycomb repression of Hox genes involves spatial
1277 feedback but not domain compaction or demixing. 2022.10.14.512199 Preprint at
1278 <https://doi.org/10.1101/2022.10.14.512199> (2022).

1279 15. King, H. W., Fursova, N. A., Blackledge, N. P. & Klose, R. J. Polycomb repressive
1280 complex 1 shapes the nucleosome landscape but not accessibility at target genes.
1281 *Genome Res.* **28**, 1494–1507 (2018).

1282 16. Chittcock, E. C., Latwiel, S., Miller, T. C. R. & Müller, C. W. Molecular architecture of
1283 polycomb repressive complexes. *Biochemical Society Transactions* **45**, 193–205 (2017).

1284 17. Gibson, B. A. *et al.* Organization of Chromatin by Intrinsic and Regulated Phase
1285 Separation. *Cell* **179**, 470-484.e21 (2019).

1286 18. Maeshima, K. *et al.* Nucleosomal arrays self-assemble into supramolecular globular
1287 structures lacking 30-nm fibers. *The EMBO Journal* **35**, 1115–1132 (2016).

1288 19. Zhang, M. *et al.* Molecular organization of the early stages of nucleosome phase
1289 separation visualized by cryo-electron tomography. *Molecular Cell* **82**, 3000-3014.e9
1290 (2022).

1291 20. Strickfaden, H. *et al.* Condensed Chromatin Behaves like a Solid on the Mesoscale In
1292 Vitro and in Living Cells. *Cell* **183**, 1772-1784.e13 (2020).

1293 21. Cai, S., Böck, D., Pilhofer, M. & Gan, L. The in situ structures of mono-, di-, and
1294 trinucleosomes in human heterochromatin. *MBioC* **29**, 2450–2457 (2018).

1295 22. Farr, S. E., Woods, E. J., Joseph, J. A., Garaizar, A. & Collepardo-Guevara, R.
1296 Nucleosome plasticity is a critical element of chromatin liquid–liquid phase separation
1297 and multivalent nucleosome interactions. *Nat Commun* **12**, 2883 (2021).

1298 23. Morey, L. *et al.* Nonoverlapping Functions of the Polycomb Group Cbx Family of
1299 Proteins in Embryonic Stem Cells. *Cell Stem Cell* **10**, 47–62 (2012).

1300 24. Chung, C.-Y. *et al.* Cbx8 Acts Non-canonically with Wdr5 to Promote Mammary
1301 Tumorigenesis. *Cell Reports* **16**, 472–486 (2016).

1302 25. Tan, J. *et al.* CBX8, a Polycomb Group Protein, Is Essential for MLL-AF9-Induced
1303 Leukemogenesis. *Cancer Cell* **20**, 563–575 (2011).

1304 26. Voss, N. R. & Gerstein, M. 3V: cavity, channel and cleft volume calculator and extractor.
1305 *Nucleic Acids Research* **38**, W555–W562 (2010).

1306 27. Hou, Z., Nightingale, F., Zhu, Y., MacGregor-Chatwin, C. & Zhang, P. Structure of native
1307 chromatin fibres revealed by Cryo-ET in situ. *Nature Communications* **14**, 6324 (2023).

1308 28. Stefan Niekamp, Sharon K. Marr, Theresa A. Oei, Radhika Subramanian, & Robert E.
1309 Kingston. Modularity of PRC1 Composition and Chromatin Interaction define
1310 Condensate Properties. *Mol Cell*. **84**, 1651-1666 (2024) doi:10.1101/2023.10.26.564217.

1311 29. Gambin, Y. *et al.* Single-Molecule Fluorescence Reveals the Oligomerization and
1312 Folding Steps Driving the Prion-like Behavior of ASC. *Journal of Molecular Biology* **430**,
1313 491–508 (2018).

1314 30. Sierecki, E. *et al.* Nanomolar oligomerization and selective co-aggregation of α -synuclein
1315 pathogenic mutants revealed by single-molecule fluorescence. *Scientific Reports* **6**,
1316 37630 (2016).

1317 31. Huseyin, M. K. & Klose, R. J. Live-cell single particle tracking of PRC1 reveals a highly
1318 dynamic system with low target site occupancy. *Nat Commun* **12**, 887 (2021).

1319 32. Barbieri, M. *et al.* Complexity of chromatin folding is captured by the strings and binders
1320 switch model. *Proceedings of the National Academy of Sciences* **109**, 16173–16178
1321 (2012).

1322 33. Erdel, F. & Rippe, K. Formation of Chromatin Subcompartments by Phase Separation.
1323 *Biophysical Journal* **114**, 2262–2270 (2018).

1324 34. Lawrimore, J. *et al.* The rDNA is biomolecular condensate formed by polymer–polymer
1325 phase separation and is sequestered in the nucleolus by transcription and R-loops.
1326 *Nucleic Acids Research* **49**, 4586–4598 (2021).

1327 35. Brown, K. *et al.* Principles of assembly and regulation of condensates of Polycomb
1328 repressive complex 1 through phase separation. *Cell Reports* **42**, (2023).

1329 36. McGinty, R. K., Henrici, R. C. & Tan, S. Crystal structure of the PRC1 ubiquitylation
1330 module bound to the nucleosome. *Nature* **514**, 591–596 (2014).

1331 37. Connelly, K. E. *et al.* Engagement of DNA and H3K27me3 by the CBX8 chromodomain
1332 drives chromatin association. *Nucleic Acids Research* **47**, 2289–2305 (2019).

1333 38. Bernstein, E. *et al.* Mouse Polycomb Proteins Bind Differentially to Methylated Histone
1334 H3 and RNA and Are Enriched in Facultative Heterochromatin. *Molecular and Cellular*
1335 *Biology* **26**, 2560–2569 (2006).

1336 39. Fleming, P. J. & Fleming, K. G. HullRad: Fast Calculations of Folded and Disordered
1337 Protein and Nucleic Acid Hydrodynamic Properties. *Biophysical Journal* **114**, 856–869
1338 (2018).

1339 40. Davies, D. R., Goryshin, I. Y., Reznikoff, W. S. & Rayment, I. Three-Dimensional
1340 Structure of the Tn5 Synaptic Complex Transposition Intermediate. *Science* **289**, 77–85
1341 (2000).

1342 41. Meléndez-Ramírez, C. *et al.* Dynamic landscape of chromatin accessibility and
1343 transcriptomic changes during differentiation of human embryonic stem cells into
1344 dopaminergic neurons. *Sci Rep* **11**, 16977 (2021).

1345 42. Suh, J. L. *et al.* Reprogramming CBX8-PRC1 function with a positive allosteric
1346 modulator. *Cell Chemical Biology* **29**, 555-571.e11 (2022).

1347 43. Seif, E. *et al.* Phase separation by the polyhomeotic sterile alpha motif
1348 compartmentalizes Polycomb Group proteins and enhances their activity. *Nat Commun*
1349 **11**, 5609 (2020).

1350 44. Gray, F. *et al.* BMI1 regulates PRC1 architecture and activity through homo- and hetero-
1351 oligomerization. *Nat Commun.* **7**, 13343 (2016).

1352 45. He, S. *et al.* Structure of nucleosome-bound human BAF complex. *Science* **367**, 875–
1353 881 (2020).

1354 46. Wang, H. *et al.* Structure of the transcription coactivator SAGA. *Nature* **577**, 717–720
1355 (2020).

1356 47. Schilbach, S., Aibara, S., Dienemann, C., Grabbe, F. & Cramer, P. Structure of RNA
1357 polymerase II pre-initiation complex at 2.9 Å defines initial DNA opening. *Cell* **184**, 4064–
1358 4072.e28 (2021).

1359 48. McCall, K. & Bender, W. Probes of chromatin accessibility in the *Drosophila* bithorax
1360 complex respond differently to Polycomb-mediated repression. *The EMBO Journal* **15**,
1361 569–580 (1996).

1362 49. Maeshima, K. *et al.* The physical size of transcription factors is key to transcriptional
1363 regulation in chromatin domains. *J. Phys.: Condens. Matter* **27**, 064116 (2015).

1364 50. Bepler, T., Kelley, K., Noble, A. J. & Berger, B. Topaz-Denoise: general deep denoising
1365 models for cryoEM and cryoET. *Nat Commun* **11**, 5208 (2020).

1366 51. Zhang, Q. *et al.* PALI1 facilitates DNA and nucleosome binding by PRC2 and triggers an
1367 allosteric activation of catalysis. *Nat Commun* **12**, 4592 (2021).

1368 52. Brzovic, P. S., Lissounov, A., Christensen, D. E., Hoyt, D. W. & Klevit, R. E. A
1369 UbcH5/Ubiquitin Noncovalent Complex Is Required for Processive BRCA1-Directed
1370 Ubiquitination. *Molecular Cell* **21**, 873–880 (2006).

1371 53. Pichler, A. *et al.* SUMO modification of the ubiquitin-conjugating enzyme E2-25K. *Nat
1372 Struct Mol Biol* **12**, 264–269 (2005).

1373 54. Uckelmann, M. *et al.* USP48 restrains resection by site-specific cleavage of the BRCA1
1374 ubiquitin mark from H2A. *Nat Commun* **9**, 229 (2018).

1375 55. Luger, K., Rechsteiner, T. J. & Richmond, T. J. Preparation of nucleosome core particle
1376 from recombinant histones. in *Methods in Enzymology* vol. 304 3–19 (Academic Press,
1377 1999).

1378 56. Sabantsev, A., Levendosky, R. F., Zhuang, X., Bowman, G. D. & Deindl, S. Direct
1379 observation of coordinated DNA movements on the nucleosome during chromatin
1380 remodelling. *Nat Commun* **10**, 1720 (2019).

1381 57. Hagen, W. J. H., Wan, W. & Briggs, J. A. G. Implementation of a cryo-electron
1382 tomography tilt-scheme optimized for high resolution subtomogram averaging. *Journal of
1383 Structural Biology* **197**, 191–198 (2017).

1384 58. Zheng, S. Q. *et al.* MotionCor2: anisotropic correction of beam-induced motion for
1385 improved cryo-electron microscopy. *Nat Methods* **14**, 331–332 (2017).

1386 59. Mastronarde, D. N. Dual-Axis Tomography: An Approach with Alignment Methods That
1387 Preserve Resolution. *Journal of Structural Biology* **120**, 343–352 (1997).

1388 60. Himes, B. A. & Zhang, P. emClarity: software for high-resolution cryo-electron
1389 tomography and subtomogram averaging. *Nat Methods* **15**, 955–961 (2018).

1390 61. Castaño-Díez, D., Kudryashev, M., Arheit, M. & Stahlberg, H. Dynamo: A flexible, user-
1391 friendly development tool for subtomogram averaging of cryo-EM data in high-
1392 performance computing environments. *Journal of Structural Biology* **178**, 139–151
1393 (2012).

1394 62. Chua, E. Y. D. *et al.* 3.9 Å structure of the nucleosome core particle determined by
1395 phase-plate cryo-EM. *Nucleic Acids Res* **44**, 8013–8019 (2016).

1396 63. Davey, C. A., Sargent, D. F., Luger, K., Maeder, A. W. & Richmond, T. J. Solvent
1397 Mediated Interactions in the Structure of the Nucleosome Core Particle at 1.9 Å
1398 Resolution††We dedicate this paper to the memory of Max Perutz who was particularly
1399 inspirational and supportive to T.J.R. in the early stages of this study. *Journal of
1400 Molecular Biology* **319**, 1097–1113 (2002).

1401 64. Kasinath, V. *et al.* Structures of human PRC2 with its cofactors AEBP2 and JARID2.
1402 *Science* **359**, 940–944 (2018).

1403 65. Chen, X. *et al.* Structures of +1 nucleosome–bound PIC-Mediator complex. *Science* **378**,
1404 62–68 (2022).

1405 66. Leitão, A. D. G. *et al.* Selectivity of Lewy body protein interactions along the aggregation
1406 pathway of α-synuclein. *Communications Biology* **4**, 1124 (2021).

1407 67. Lau, D. *et al.* Single Molecule Fingerprinting Reveals Different Amplification Properties of
1408 α-Synuclein Oligomers and Preformed Fibrils in Seeding Assay. *ACS Chem. Neurosci.*
1409 **13**, 883–896 (2022).

1410 68. Bhumkar, A. *et al.* Single-Molecule Counting Coupled to Rapid Amplification Enables
1411 Detection of α -Synuclein Aggregates in Cerebrospinal Fluid of Parkinson's Disease
1412 Patients. *Angewandte Chemie International Edition* **60**, 11874–11883 (2021).

1413 69. Horn, V. *et al.* Structural basis of specific H2A K13/K15 ubiquitination by RNF168. *Nat
1414 Commun* **10**, 1751 (2019).

1415 70. Yang, B. *et al.* Identification of cross-linked peptides from complex samples. *Nat
1416 Methods* **9**, 904–906 (2012).

1417 71. Gail, E. H., Shah, A. D., Schittenhelm, R. B. & Davidovich, C. crisscrosslinkeR:
1418 identification and visualization of protein–RNA and protein–protein interactions from
1419 crosslinking mass spectrometry. *Bioinformatics* **36**, 5530–5532 (2020).

1420 72. Combe, C. W., Fischer, L. & Rappsilber, J. xiNET: Cross-link Network Maps With
1421 Residue Resolution*. *Molecular & Cellular Proteomics* **14**, 1137–1147 (2015).

1422 73. Canver, M. C. *et al.* A saturating mutagenesis CRISPR-Cas9–mediated functional
1423 genomic screen identifies cis- and trans-regulatory elements of Oct4 in murine ESCs.
1424 *Journal of Biological Chemistry* **295**, 15797–15809 (2020).

1425 74. Seruggia, D. *et al.* TAF5L and TAF6L Maintain Self-Renewal of Embryonic Stem Cells
1426 via the MYC Regulatory Network. *Molecular Cell* **74**, 1148-1163.e7 (2019).

1427 75. Healy, E. *et al.* PRC2.1 and PRC2.2 Synergize to Coordinate H3K27 Trimethylation.
1428 *Molecular Cell* **76**, 437-452.e6 (2019).

1429 76. Martin, M. Cutadapt removes adapter sequences from high-throughput sequencing
1430 reads. *EMBnet.journal* **17**, 10–12 (2011).

1431 77. Langmead, B. & Salzberg, S. L. Fast gapped-read alignment with Bowtie 2. *Nat Methods*
1432 **9**, 357–359 (2012).

1433 78. Zhang, Y. *et al.* Model-based Analysis of ChIP-Seq (MACS). *Genome Biology* **9**, R137
1434 (2008).

1435 79. Amemiya, H. M., Kundaje, A. & Boyle, A. P. The ENCODE Blacklist: Identification of
1436 Problematic Regions of the Genome. *Sci Rep* **9**, 9354 (2019).

1437 80. Reske, J. J., Wilson, M. R. & Chandler, R. L. ATAC-seq normalization method can
1438 significantly affect differential accessibility analysis and interpretation. *Epigenetics &*
1439 *Chromatin* **13**, 22 (2020).

1440 81. Zhu, L. J. *et al.* ChIPpeakAnno: a Bioconductor package to annotate ChIP-seq and
1441 ChIP-chip data. *BMC Bioinformatics* **11**, 237 (2010).

1442